Spatiotemporal recruitment of the ubiquitin-specific protease USP8 directs endosome maturation

Yue Miao[1,2#], Yongtao Du[1,2#], Baolei Wang[1,2], Jingjing Liang[1], Yu Liang[1,2], Song Dang[1], Jiahao Liu[2,3], Dong Li[2,3], Kangmin He[1,2]*, Mei Ding[1,2]*

[1] State Key Laboratory of Molecular Developmental Biology, Institute of Genetics and Developmental Biology, Chinese Academy of Sciences, Beijing 100101, China

[2] University of Chinese Academy of Sciences, Beijing 100049, China

[3]National Laboratory of Biomacromolecules, CAS Center for Excellence in Biomacromolecules, Institute of Biophysics, Chinese Academy of Sciences, Beijing 100101, China

[#] These authors contributed equally to this work.

*kmhe@genetics.ac.cn (KH); mding@genetics.ac.cn (MD)

Abstract

The spatiotemporal transition of small GTPase Rab5 to Rab7 is crucial for early-to-late endosome maturation, yet the precise mechanism governing Rab5-to-Rab7 switching remains elusive. USP8, a ubiquitin-specific protease, plays a prominent role in the endosomal sorting of a wide range of transmembrane receptors and is a promising target in cancer therapy. Here, we identified that USP8 is recruited to Rab5-positive carriers by Rabex5, a guanine nucleotide exchange factor (GEF) for Rab5. The recruitment of USP8 dissociates Rabex5 from early endosomes (EEs) and meanwhile promotes the recruitment of the Rab7 GEF SAND-1/Mon1. In USP8-deficient cells, the level of active Rab5 is increased, while the Rab7 signal is decreased. As a result, enlarged EEs with abundant intraluminal vesicles accumulate and digestive lysosomes are rudimentary. Together, our results reveal an important and unexpected role of a deubiquitinating enzyme in endosome maturation.

Introduction

Endosomes are dynamic and heterogeneous organelles that act as hubs for endocytic trafficking, recycling and degradation. During endocytosis, membrane proteins marked by ubiquitination are incorporated into endocytic vesicles and then transported to early endosomes (EEs). At EEs, membrane proteins are either brought to the recycling endosomes (REs) or incorporated into intraluminal vesicles (ILVs) with the help of ESCRT (Endosomal Sorting Complex Required for Transport) complexes (Sardana and Emr, 2021). The ILV-containing compartments, often referred to multivesicular bodies (MVBs), are more acidified and upon fusion with lysosomes, can deliver both transmembrane cargos for degradation, as well as fresh supplies of lysosomal hydrolase enzymes required for the turnover of proteins, lipids and other cellular components (Huotari and Helenius, 2011; Sardana and Emr, 2021). The EE-to-MVB endosome maturation process is mainly controlled by endosome-specific Rab GTPases and phosphoinositides (Borchers et al., 2021; Huotari and Helenius, 2011; Kümmel et al., 2023; Stenmark, 2009). Rab GTPases are guanine nucleotide binding proteins that switch between an inactive GDP-bound and an active GTP-bound state. Within the cytosol, the GDP-bound Rab proteins are kept soluble by binding to the GDP dissociation inhibitor (GDI). The GTP-bound Rabs, activated by their corresponding GEF, can associate with cellular membranes and recruit effector proteins.

Rab5, the Rab GTPase critical for early endosome formation and function, can be activated and recruited to EEs by its GEF, Rabex5 (Mattera and Bonifacino, 2008; Zhu et al., 2007). The GTP-bound active Rab5 recruits its effectors, for instance, Rabaptin-

5. Rabaptin-5 in turn binds to Rabex5 via a coiled-coil region, resulting in a positive feedback loop of Rab5 activation on endosomal membranes (Zhang et al., 2014b). Isolated Rabex5 appears to have relatively low GEF activity *in vitro* (Delprato and Lambright, 2007) and binding of Rabaptin-5 to Rabex5 causes a rearrangement in the Rabex5 C-terminus and subsequently enhances nucleotide exchange of Rab5 (Horiuchi et al., 1997; Lauer et al., 2019; Lippé et al., 2001; Zhang et al., 2014b). Thus, autoinhibition likely serves as a key regulatory mechanism in controlling GEF activity. Other effectors of Rab5 include the phosphatidylinositol-3-phosphate (PI3P) kinase complex II (VPS34/VPS15/Beclin 1/UVRAG) (Tremel et al., 2021), which promotes the synthesis of phosphatidylinositol-3-phosphate (PI3P) on endosomes, and the class C core vacuole/endosome tethering (CORVET) complex, which promotes membrane homotypic fusion (Abenza et al., 2010; Balderhaar et al., 2013; Peplowska et al., 2007). Rab5 also recruits the early endosomal antigen 1 (EEA1), a tethering protein required for fusion of endocytic vesicles with EEs (Christoforidis et al., 1999). The phosphorylated head group of PI3P binds to specific domains, such as the FYVE domain in EEA1, allowing for the organelle-specific association of proteins containing this domain (Lawe et al., 2002; Stenmark et al., 1996). The fusion of vesicles with organelles depends on tethering complexes as well as soluble *N*-ethylmaleimide-sensitive factor attachment protein receptors (SNAREs). Reconstitution of early endosome fusion revealed that EEA1 functions in the context of multiple additional components, including endosomal SNAREs, during fusion (Ohya et al., 2009). Rab5 effectors also include the Rab7 GEF Mon1–Ccz1 complex. Rab7 activation by Mon1-

Ccz1 complex is essential for the biogenesis and positioning of late endosomes (LEs) and lysosomes, and for the fusion of endosomes and autophagosomes with lysosomes. The Mon1–Ccz1 complex is a heterodimer in yeast, and a heterotrimer in metazoan cells (Dehnen et al., 2020; Vaites et al., 2018; van den Boomen et al., 2020; Wang et al., 2002). The activation of Mon1-Ccz1 is depended on Rab5 interaction (Borchers et al., 2023; Langemeyer et al., 2020) and Mon1 also coordinates endosome maturation together with the Rab5 GAP TBC1D18 (Hiragi et al., 2022). Additionally, the Mon1-Ccz1 complex is able to interact with Rabex5 (Poteryaev et al., 2010), causing dissociation of Rabex5 from the membrane, which probably terminates the positive feedback loop of Rab5 activation and then promotes the recruitment and activation of Rab7 on endosomes (Nordmann et al., 2010; Poteryaev et al., 2010). All in all, the hierarchy of protein recruitment and their reciprocal regulation ensures the rapid transition from Rab5- to Rab7-positive vesicles which is critical for endosome maturation.

The conserved ESCRT machinery drives endosomal membrane deformation and scission leading to the formation of ILVs within MVBs. On the surface of endosomes, ESCRT-0, -I and -II bind to ubiquitinated membrane proteins, while ESCRT-III and Vps4 bud ILVs into the lumen of the endosomes (Wollert and Hurley, 2010). The deubiquitinating enzyme (DUB) USP8 belongs to the ubiquitin-specific protease (USP) family and plays a prominent role in the regulation of endosomal sorting of a wide range of transmembrane receptors (Dufner and Knobeloch, 2019). In addition to direct deubiquitination, USP8 also regulates protein stability through its interactions with

various ESCRT components. By binding to STAM and Hrs, USP8 stabilizes the ESCRT-0 complex, which is the crucial element directing ubiquitinated substrates towards MVB/lysosome-mediated degradation (Mizuno et al., 2006; Row et al., 2006). The N-terminal microtubule interacting and transport (MIT) domain of USP8 interacts with ESCRT-III proteins, which are thought to be the driving force of several membrane scission events (Row et al., 2007). In the absence of USP8, EGFR is abnormally accumulated in EEs (Alwan and van Leeuwen, 2007; Row et al., 2006). Additionally, the endocytic trafficking of the Frizzled receptor, Smooth, as well as key components of the Wnt and Hedgehog pathways is also affected by *usp8* deficiency (Ali et al., 2013; Berlin et al., 2010a; Berlin et al., 2010b; Crespo-Yàñez et al., 2018; Jacomin et al., 2015; MacDonald et al., 2014). Noticeably, however, the impact of USP8 on protein stability is highly variable and sometimes controversial (Berlin et al., 2010b; Mizuno et al., 2005; Niendorf et al., 2007; Row et al., 2006).

Here, utilizing both *C. elegans* and cultured mammalian cells as models, we identified that USP8 is recruited to Rab5-positive vesicles through Rabex5 and functions through both the endosomal dissociation of Rabex5 and recruitment of SAND-1/Mon1 to promote endosome maturation. USP8 has recently arisen as a promising therapeutic target in at least two distinct pathological contexts associated with USP8 overexpression or gain-of-function variants (Dufner and Knobeloch, 2019; Li et al., 2024; Reincke et al., 2015). Thus, our data reveal an important and direct role of USP8 in endosome maturation and have clear implications for the therapeutic treatment of USP8-related human diseases.

Results

usp-50 mutation leads to reduction of lysosomal compartments and enlarged MVB-like structures

The epithelial cell hyp7 (hypodermal cell 7) covers most of the worm body and is the largest cell in *C. elegans*. When fused to GFP and driven by the *ced-1* promoter, the transmembrane lysine/arginine transporter LAAT-1 can be used to highlight the lysosome structures in the hyp7 cell (Figure 1A) (Liu et al., 2012). In wild type, as worms mature from L4 (larval stage 4) to adult stage, the vesicular and tubular structures of lysosomes become enlarged (Figure 1A) (Sun et al., 2020). In *usp-50(xd413)*, a recessive mutation isolated from a genetic screen of worms mutagenized with EMS (ethylmethane sulfonate), lysosomes appear to be greatly reduced in size (Figure 1B and D). For another *usp-50* allele, *gk632973*, the lysosome distribution and morphology appear normal during L4 stage (Figure 1C). However, when *usp-50(gk632973)* animals reach adult stage, the individual size and total volume of lysosomes are also reduced (Figure 1C and D). *nuc-1* encodes a lysosomal deoxyribonuclease (Wu et al., 2000). In *usp-50(xd413)* animals, the NUC-1 protein is properly targeted to LAAT-1-containing vesicles (Figure 1E and F; and Figure1-figure supplement 1A), which indicates that the assembly of *de novo* lysosomes is not affected by *usp-50*.

usp-50 encodes the *C. elegans* homolog of *S. cerevisiae* Doa4p and human USP8/UBPY (Bowers et al., 2004; Huynh et al., 2016). All the USP8 family members

contain a UCH domain which is crucial for the deubiquitination activity (Komander et al., 2009). The molecular lesions of both *usp-50(xd413)* and *usp-50(gk632973)* occur in the UCH domain, leading to a G541A and A523V substitution respectively. USP8 was identified as a protein associated with ESCRT components (Kato et al., 2000; Mathieu et al., 2022; Row et al., 2007). The ESCRT machinery drives endosomal membrane deformation and scission, leading to the formation of ILVs within MVBs (Babst, 2011; Wollert and Hurley, 2010). To address whether the reduced lysosomal structures in *usp-50* animals are linked to MVB formation, we performed the following experiments. Firstly, we examined the cellular localization of the two ESCRT-0 components, HGRS-1 and STAM-1. In wild-type animals, both HGRS-1::GFP and STAM-1::GFP are distributed in a distinct punctate pattern (Figure 1G and H). When *usp-50* is mutated, the HGRS-1::GFP and STAM-1 signals are greatly reduced (Figure 1G and H; and Figure1-figure supplement 1B), which is consistent with the role of USP8 in stabilizing the ESCRT-0 complex (Kato et al., 2000; Mizuno et al., 2006; Niendorf et al., 2007; Row et al., 2006; Zhang et al., 2014a). Next, we prepared high-pressure frozen samples and performed transmission electron microscopy (TEM) analysis to examine MVB formation in worm epidermal cells. In wild type, the characteristic MVBs (Fig. 1 I and I') are rare and difficult to detect, and the diameter of those MVBs ranges from 0.1 μm to 0.5 μm (Fig. 1 J). Intriguingly, we identified many more vesicles with various membranous contents in *usp-50(xd413)* mutants. The average size of those *usp-50* mutant vesicles is significantly larger than wild type (Figure 1J-N). Based upon the vesicular inclusions, we divided those abnormally

enlarged vesicles into four categories. The first class is composed of vesicles containing abundant ILV-like structures (Figure 1K). About 58.7% of the abnormal vesicles belong to this category. The second class (26.8%) includes vesicles filled with threadlike membrane structures (Figure 1L). Vesicles of the third type (22.4%) are loaded with threadlike membrane structures and electron-dense material (Figure 1M). The fourth class, which accounts for a relatively small proportion of mutant vesicles (4.9%), contains various cellular organelles, for instance mitochondria (Figure 1N). Together, the reduction of ESCRT-0 components and accumulation of abnormal enlarged vesicles indicate that USP-50 functions in concert with ESCRT complex to regulate endolysosomal trafficking.

Enlarged EEs in *usp-50/usp8* mutant cells

Lysosomes receive and digest materials generated by endocytic pathways. Considering the much reduced lysosome structures in *usp-50* mutants, we wondered whether the abnormally enlarged vesicular structures are actually homotypic fusion products of EEs. Using YFP-tagged 2xFYVE (YFP::2xFYVE), which specifically labels PI3P, we examined the size and morphology of EEs (Figure 2A). We found that the size of individual EEs is significantly increased (Figure 2B). Meanwhile, the total volume of EEs in *usp-50* mutants remains similar to wild type (Figure 2B), implying that the homotypic fusion of EEs is probably increased. The enlarged EEs in *usp-50(xd413)* are not coated with the lysosome marker LAAT-1::mCherry (Figure 2C and D; and Figure 2-figure supplement 1A). Hence, the EEs remain differentiated from lysosome

structures. The enlarged early endosome defect in *usp-50(xd413)* mutants is rescued by either worm *usp-50* or human USP8 (Figure 2J; and Figure 2-figure supplement 1B), which suggests that the function of USP-50/USP8 is evolutionarily conserved. Indeed, when we knocked out the expression of USP8 (USP8-KO) in human breast cancer SUM159 cells (Figure 2-figure supplement 1C), the transient expression of EGFP-2xFYVE confirmed that USP8 depletion caused early endosome enlargement (Figure 2K).

There was no obvious alteration in the pattern of reporters for Golgi apparatus (MANS::GFP), retromers (VPS-29::GFP), or recycling endosomes (GFP::RME-1) (Figure 2-figure supplement 2). This suggests that the endolysosomal trafficking process is rather specifically affected by *usp-50*.

USP8 is dynamically recruited to Rab5-positive vesicles

How does USP-50/USP8 control the size of EEs? To address this question, we firstly analyzed the subcellular localization of USP-50/USP8. In worm epidermal cells, the GFP-tagged USP-50 protein is co-localized with mCherry::RAB-5 (Figure 3-figure supplement 1A) but not with mCherry::RAB-7 (Figure 3-figure supplement 1B), consistent with the early endosomal localization of USP-50/USP8 (Mizuno et al., 2005; Row et al., 2006). The catalytic ubiquitin C-terminal hydrolase (UCH) domain possesses a “cysteine box” containing the active site residues, including Cysteine 492 (C492) (Naviglio et al., 1998). When we mutated C492 to Alanine, we found that the GFP-tagged USP-50(C492A) protein is still co-localized with mCherry::RAB-5

(Figure 3-figure supplement 1C). Thus, the EE localization of USP-50 is not dependent on its deubiquitination activity. Meanwhile, the mCherry::RAB-5 signal is strongly enhanced by the overexpression of USP-50(C492A) (Figure 3-figure supplement 1C), suggesting that the C492A mutation may have a dominant-negative effect on USP-50 function.

To reveal the subcellular localization of USP8 in mammalian cells, we used the CRISPR/Cas9 approach to generate a SUM159 cell line in which the endogenous USP8 was tagged with mEGFP (USP8-mEGFP$^{+/+}$) (Figure 3-figure supplement 2). As shown in Figure 3, USP8-mEGFP co-localizes well with the EE marker mScarlet-I-EEA1 (Figure 3A). In contrast, LE or lysosome markers, including mScarlet-I-Rab7a and Lamp1-mScarlet-I, have little overlap with the USP8-mEGFP signal (Figure 3B and C). Constitutively activated Rab5 GTPase (Rab5c-Q80L) causes enlarged EEs (Stenmark et al., 1994; Wegner et al., 2010). Instead of being evenly distributed, USP8-mEGFP formed individual spots located on one side of the enlarged endosomes (Figure 3D). We further analyzed the sub-organelle distribution of USP8 using structured illumination microscopy (SIM). Consistent with what we observed in enlarged EEs caused by Rab5c-Q80L overexpression, the USP8-mEGFP dots indeed located at subdomains of EEs (Figure 3E). The uneven distribution of USP8 implies that USP8 may associate dynamically with EEs. To further investigate the dynamic association of USP8 with EEs, we transiently expressed mScarlet-I-Rab5c in the genome-edited USP8-mEGFP$^{+/+}$ cells and tracked the recruitment dynamics of USP8-mEGFP to EEs by spinning-disk confocal microscopy (Figure 3F). We previously reported that Rab5

was recruited to nascent endocytic carriers following the un-coating of clathrin-coated vesicles (He et al., 2017). This recruitment resulted in the creation of Rab5-positive endocytic carriers, which could subsequently fuse with other Rab5-positive endocytic carriers or EEA1-positive EEs (He et al., 2017). We found that USP8-mEGFP was recruited to these nascent mScarlet-I-Rab5c-positive vesicles which appeared around the bottom surface of the cells (Figure 3F). Additionally, we observed the dynamic appearance and disappearance of single USP8-mEGFP spots on these large Rab5c-positive endosomes (Figure 3G-H).

USP-50/USP8 recruitment dissociates RABX-5 from endosomes

How is the endosomal recruitment of USP8 related to its function in endolysosomal trafficking process? By searching the putative USP-50 binding partners, we found that USP-50 can bind to RABX-5, the worm homolog of Rabex5 protein (Figure 4A and B). To determine which domain of RABX-5 is required for the interaction with USP-50, we constructed a panel of FLAG-tagged RABX-5 truncation mutants (Figure 4C) and performed a series of immunoprecipitation tests (Figure 4D). In general, the C-terminal coiled-coil (CC) and the C-terminal proline-rich (PR) domains are sufficient for RABX-5 to interact with USP-50. Meanwhile, the N-terminal region, including an A20-zinc finger domain (ZF), a motif interacting with ubiquitin (U), the membrane-binding motif (MB) and the downstream helical bundle domain (HB) of RABX-5 could also mediate USP-50 binding. Further including Vps9 domain enhances the molecular interaction between RABX-5 and USP-50 (Figure 4C and D).

Does RABX-5 binding affect the endosomal localization of USP-50? To address this question, we created a molecular null of *rabx-5* using the CRISPR/Cas9 technique (Dickinson et al., 2013) (Figure 4E). The *rabx-5(null)* animals are healthy and fertile and do not display obvious morphological or behavioral defects. In *rabx-5(null)* mutant animals, the punctate USP-50::GFP signal becomes diffusely distributed (Figure 4F and G). Thus, *rabx-5* is require for the endosomal localization of USP-50.

What is the biological significance of RABX-5-mediated USP-50 recruitment? In wild-type animals, the fluorescence signal of RABX-5::GFP KI in hyp7 is rather dim (Figure 5A). When *usp-50* is mutated, the RABX-5::GFP KI signal is greatly enhanced (Figure 5B). USP8-KO also caused a significant increase in the number of enlarged endosomes in Rabex5-mEGFP$^{+/+}$ SUM159 cells (Figure 5-figure supplement 1A-C and E). Rabex5-mEGFP signals were enriched and co-localized well with the mScarlet-I-Rab5c signal on the enlarged endosomes (Figure 5-figure supplement 1A). Antibody staining of endogenous EEA1 further showed that the enlarged EEs in USP8-KO cells were coated with both Rabex5 and EEA1 (Figure 5-figure supplement 1D). The increased endosomal RABX-5/Rabex5 may lead to Rab5 signal enhancement. Indeed, in *usp-50* mutants, the GFP::RAB-5 KI-labeled vesicles are significantly enlarged (Figure 5-figure supplement 2A-C) and the proportion of membrane-associated GFP::RAB-5 KI is also increased (Figure 5-figure supplement 2D). The GTP-bound activated RAB-5 protein binds to its downstream effector EEA1 via the N-terminal domain of EEA1 (EEA1-NT). We utilized EEA1-NT (Figure 5-figure supplement 2E) to show that loss of *usp-50* indeed led to more activated RAB-5 *in vivo* (Figure 5-figure

supplement 2F). In addition, the total RAB-5 protein level is increased by *usp-50* mutation (Figure 5-figure supplement 2G and H), which implies that RAB-5 activation may stabilize RAB-5 protein. To explore the relationship between Rab5 and USP8 in SUM159 cells, we knocked down the expression of USP8 by siRNA (USP8-KD) in the clonal genome-edited EGFP-Rab5c$^{+/+}$ cells. We found that EEs, labeled by Rab5, are significantly enlarged (Figure 5-figure supplement 2I and J). Taken together, these results indicate that USP-50/USP8 recruitment dissociates RABX-5 from endosomes, and subsequently diminish Rab5 signaling.

USP-50 acts on K323 de-ubiquitination to regulate RABX-5 localization

The enzyme-inactive USP-50(C492A) cannot rescue the enhanced endosomal RABX-5 signal in *usp-50* mutant animals (Figure 5C and D). This suggests that USP-50 acts through its de-ubiquitination activity to dissociate RABX-5 from endosomes. To further dissect how the USP-50-mediated de-ubiquitination might contribute to RABX-5 localization, we precipitated the FLAG-tagged RABX-5 from overexpressed 293T cells and performed ubiquitination proteomics analysis. We found that the K88 and K323 residues of RABX-5 are modified by ubiquitin *in vivo* (Figure 5-figure supplement 3A and B). K88 is located in the membrane-binding motif, while K323 resides in the conserved Vps9 domain of RABX-5 (Figure 5-figure supplement 3B). To understand whether and how these two ubiquitin modification sites are involved in USP-50-mediated deubiquitination, we generated non-ubiquitinated mutations at K88 and K323 (K88R and K323R, respectively). In wild-type animals, the RABX-5::GFP KI intensity

is rather dim (Figure 5A). When *usp-50* is mutated, the RABX-5::GFP KI intensity is strongly enhanced and displays the typical punctate pattern (Figure 5B and I). On a wild-type background, both RABX-5(K88R)::GFP KI and RABX-5(K323R)::GFP KI display weak signals (Figure 5E and G) similar to wild-type RABX-5::GFP KI (Figure 5A). When *usp-50* is mutated, the RABX-5(K88R)::GFP KI signal is greatly enhanced and displays an apparent punctate pattern (Figure 5F and I), which is similar to what we observed with the wild-type RABX-5::GFP KI line. In contrast, when K323 is mutated, the signal from RABX-5(K323A)::GFP KI remains dim in both wild-type and *usp-50* mutant animals (Figure 5G-I). These observations suggest that USP-50 cannot regulate the endosomal localization of RABX-5 when K323 is mutated. Furthermore, the *rabx-5(K323R)* mutation successfully suppressed both the enlarged early endosome and diminished late endosome phenotypes of *usp-50* (Figure 5J-M). Taken together, USP-50 recruitment to EEs relies on RABX-5, and through its deubiquitination action on the Vps9 domain of RABX-5, USP-50 dissociates RABX-5 from EEs, thereby terminating Rab5 signaling to promote endosome maturation.

USP-50/USP8 is required for SAND-1/Mon1 recruitment

SAND-1/Mon1-Ccz1 binds to RABX-5, and by displacing RABX-5 from the endosomal membrane, functions as a GEF of Rab7 to recruit and activate Rab7 GTPase (Nordmann et al., 2010; Poteryaev et al., 2010). In the absence of RABX-5 *(rabx-5 null*), the GFP::SAND-1 puncta are diminished (Figure 6A, B and D) and the LAAT-1::GFP-labeled lysosome structures are also reduced (Figure 6E and F; and Figure 6-

figure supplement 1A). In *usp-50* mutants, the RABX-5 signal is enhanced, while the lysosome structures are reduced. Intriguingly, when we introduced the GFP::SAND-1 marker into *usp-50* mutants, we found that the punctate distribution of GFP::SAND-1 is lost (Figure 6A, C and D). Mon1a and Mon1b are mammalian homologs of worm SAND-1. In SUM159 cells, mEGFP-tagged endogenous Mon1a (Figure 6-figure supplement 1B) is localized on both Rab5-positive EEs and Rab7-positive late endosomes (Figure 6-figure supplement 1C and D). In contrast, endogenous Mon1b (Figure 6-figure supplement 1E) is more localized on late endosomes (Figure 6-figure supplement 1F and G). When the expression of USP8 in the mEGFP-Mon1a$^{+/+}$ or mEGFP-Mon1b$^{+/+}$ cells was knocked down by siRNA, we found that the number of vesicles positive for mEGFP-Mon1a or mEGFP-Mon1b was greatly reduced (Figure 6-figure supplement 1H and I). Taken together, these results indicate that the function of USP8/USP-50 in endosomal localization of SAND-1/Mon1-Ccz1 is evolutionarily conserved. We noticed that when *sand-1* is mutated, the EEs are enlarged (Figure 6J-L and Figure 6-figure supplement 1H) and late endosomes/lysosomes become smaller (Figure 6M-O and Figure 6-figure supplement 1I), which is highly similar to *usp-50* mutants. Furthermore, co-IP experiments indicated that the USP-50 protein is able to bind to SAND-1 (Figure 6P), which is consistent with the role of USP-50 in endosomal localization of SAND-1.

SAND-1/Mon1 is a GEF for Rab7, and therefore a reduced level of SAND-1/Mon1 may decrease the endosomal distribution of Rab7 (Hiragi et al., 2022; Nordmann et al., 2010; Yong et al., 2023). Indeed, with the GFP::RAB-7 KI line, we found that the

punctate RAB-7 signal was greatly reduced by loss of function of *sand-1* (Figure 6Q and R). In *usp-50* mutants, the punctate GFP::RAB-7 KI signal is also reduced (Figure 6S and T). Given the coupled phenotype of enlarged EEs and smaller late endosomes/lysosomes in both *usp-50* and *sand-1* mutants, we wondered whether increasing Rab7 would enhance the endosome maturation process, thus overriding the early endosome enlargement defect in *usp-50* mutants. Therefore, we overexpressed the wild-type *rab-7* gene and found that the early endosome enlargement phenotype of *usp-50* mutants was greatly suppressed (Figure 6U-X). In conclusion, we propose that the recruitment of USP-50/USP8, dependent on Rabex5, dissociates Rabex5 from EEs. Concurrently, this recruitment promotes the enrollment of SAND-1/Mon1-Ccz1, thereby facilitating the maturation of endosomes (Figure 6Y).

Discussion

In this study, we identified that the recruitment of ubiquitin-specific protease USP-50/USP8 to EEs requires Rabex5. Instead of stabilizing Rabex5, the USP-50/USP8 recruitment dissociates Rabex5 from endosomes and meanwhile enrolls the Rab7 GEF SAND-1/Mon1. In *usp-50/usp8* loss-of-function cells, the RABX-5/Rabex5 signal is enhanced and the SAND-1/Mon1 protein fails to be localized onto endosomes. As a result, endolysosomal trafficking is blocked and enlarged ILV-containing vesicles accumulate. Meanwhile, the lysosomal structures become rudimentary.

Most studies of USP8 focus on endosomal trafficking of growth factor receptor tyrosine kinases (RTKs) in cultured vertebrate cells. In some cases, reduced USP8

activity results in accumulation of ubiquitinated cargos (Alwan and van Leeuwen, 2007; Bowers et al., 2006; Mizuno et al., 2006; Row et al., 2006). USP8 can also promote RTK stability (Berlin et al., 2010b; Mizuno et al., 2005; Niendorf et al., 2007). It is thought that USP8 promotes the recycling of cell surface receptors back to the plasma membrane or enhances their degradation depending on when and where it deubiquitinates its substrate along the recycling pathway (Mizuno et al., 2005; Niendorf et al., 2007; Wright et al., 2011). Besides EGFR, USP8 regulates the endocytic trafficking and/or stability of many other transmembrane proteins (Martín-Rodríguez et al., 2020; Peng et al., 2020; Sun et al., 2018; Xie et al., 2022; Xiong et al., 2022), but conclusions about the impact of USP8 on protein stability are highly diverse. The conflicting results may be caused by massive global ubiquitination and proteolytic stress triggered by depletion of USP8 or overexpression of a catalytically inactive enzyme.

Endosome maturation controls the sorting, processing, recycling, and degradation of incoming substances and receptors, and is thus responsible for regulation and fine-tuning of numerous pathways in cells. The Rab5 GEF Rabex5 can be recruited to EEs through an early endosomal targeting (EET) domain or by binding with ubiquitinated cargoes through its UBD region (Mattera and Bonifacino, 2008; Zhu et al., 2007). Notably, complex intramolecular interactions are extensively involved in Rabex5 function and dynamic localization (Lauer et al., 2019). Here, RABX-5 associates with USP-50 through multiple domains. Thus, in the context of *usp8/usp-50* deletion, the enhanced endosomal localization of Rabex5/RABX-5 may be caused by alterations in

multiple inter- and intramolecular interactions. The GTP-bound active Rab5 recruits Rabaptin-5 resulting in a positive feedback loop of Rab5 activation on endosomal membranes (Zhang et al., 2014b). How is this positive feedback loop terminated? The role of Rabex5 in recruiting Rab7 GEF SAND-1/Mon1-Ccz1 is well established. Here, we further showed that the endosomal localization of USP-50 is also dependent on RABX-5. Thus, Rabex5 may recruit multifaceted negative regulators, which work subsequently or collaboratively to regulate endosome maturation. Late endosomes transport new lysosomal hydrolases and membrane proteins to lysosomes for the maintenance and amplification of the degradative compartment (Yang and Wang, 2021). Loss of worm *usp-50* results in reduced lysosome size. Previous studies also observed lysosome formation deficiency in fly *ubpy/usp8* knock-down fat cells (Jacomin et al., 2015; Jacomin et al., 2016). Removal of Rab5 and its replacement with Rab7 is an essential step in late endosome formation and in the transport of cargo to lysosomes (Borchers et al., 2021; Zeigerer et al., 2012). In the absence of USP8/USP-50, the RABX-5/Rabex5 signal is enhanced, but the endosomal localization of SAND-1/Mon1 is reduced, suggesting that in addition to Rabex5, USP8 is further needed to engage Rab7 GEF. The Mon1-Ccz1 complex can be recruited to various organelles through a variety of binding partners (Gao et al., 2018). Thus, recruited by Rabex5, USP8 may serve a linker specifically bridging endosomes to the Rab7 GEF. *sand-1* mutants display an almost identical phenotype to *usp-50* mutants, including enlarged EEs and much smaller late endosomes/lysosomes, implying that USP8/USP-50 functions similarly to SAND-1/Mon1-Ccz1. In *usp-50* mutants, the great reduction of

RAB-7 signal is accompanied by a dramatically increased RAB-5 signal. Therefore, we suspect that the extended Rab5 activation in *usp-50* mutants actually prevents the Rab5-to-Rab7 conversion from occurring. Of course, we cannot rule out the possibility that the remaining SAND-1 is able to convert some of the Rab5 to Rab7, thus forming late endosomes to some degree. However, due to the quick conversion of late endosomes to lysosomes for degradation, most of the EEs remain clearly differentiated from late endosomes/lysosomes (Figure 2C and D; and Figure 2-figure supplement 1A). Overexpression of RAB-7 rescued the enlarged early endosome phenotype of *usp-50* mutants (Fig. 6 U-X), further supporting the idea that USP-50/USP8 downregulates Rab5 signaling and meanwhile promotes Rab7 activation, thus facilitating the EE-to-MVB conversion. Giving the almost identical phenotype of *usp-50/usp8* and *sand-1/Mon1* mutants and the consecutive actions of Rab5, USP8, and Rab7, we propose a working model, in which Rab5-coated vesicles recruit USP8, possibly through RABX-5-USP-50 interactions. Subsequently, USP8 dissociates Rabex5 from endosomes, meanwhile facilitating the recruitment of SAND-1/Mon1-Ccz1 complex to initiate MVB/late endosome formation (Fig. 6, Y).

Formation of ILVs is a hallmark of MVBs, which constitute morphologically distinct late endosomal structures that receive cargo in transit to the lysosomes. USP8 is important for the stability and ubiquitination status of various ESCRT components (Adoro et al., 2017; Crespo-Yàñez et al., 2018; Mathieu et al., 2022; Mizuno et al., 2006; Niendorf et al., 2007; Zhang et al., 2014a). Indeed, the punctate distribution of ESCRT-0 components is reduced significantly in *usp-50* worms (Figure 1G-H; and

Figure 1-figure supplement 1B). By EM ultrastructural analysis, we further found that a large number of abnormal vesicular structures accumulate in *usp-50* mutants. A large portion of these enlarged vesicles contain ILV-like structures (Fig. 1, I-N). Notably, a previous study reported that even though the morphology of endocytic structures is altered dramatically in mammalian cells depleted of key subunits of all four ESCRT components, MVBs can still form (Stuffers et al., 2009). Hence, the MVB-like structures in *usp-50* mutants may be formed through pathways independent from ESCRT (Babst, 2011; Theos et al., 2006). Alternatively, the formation of ILVs may be delayed but not totally blocked by *usp-50* mutation. The impaired endosome maturation actually suppresses the ILV formation deficiency in *usp-50* mutants. In wild-type animals, MVBs are rare and hard to find, which suggests that once formed, MVBs quickly fuse with lysosomes and get degraded. Loss of *usp-50* leads to the upregulation of Rab5 signaling, and early endosomal structures cannot progress to late endosomes, and thus to degradative lysosomes, on time. When *usp-50* is mutated, the aberrantly extended early endosome status allows the delayed ILV formation to proceed, so that MVB-like structures are eventually formed. We noticed that the MVB-like vesicles in *usp-50* mutant animals are much larger than those in wild type. Considering that Rab7 is greatly reduced and the lysosome structures are much smaller, the abnormally enlarged MVB-like structures in *usp-50* mutants are likely the homotypic fusion products from RAB-5-positive EEs.

USP8 deubiquitinates numerous plasma membrane receptors, making this enzyme a promising target in cancer therapy to overcome chemoresistance associated with RTK

stabilization (Byun et al., 2013; Islam et al., 2021). Gain-of-function mutations of USP8 have been found in microadenomas of patients with Cushing's disease, a rare disease where the secretion of large amounts of adrenocorticotrophic hormone (ACTH) by pituitary corticotroph adenomas results in an excess of glucocorticoids and hypercortisolism, putatively due to defective EGFR sorting (Ma et al., 2015; Reincke et al., 2015). The role of USP8 in directing endosomal trafficking revealed here should shed new light on understanding its contribution to membrane receptor trafficking, resistance to chemotherapy, or EGFR stabilization in Cushing's disease.

Materials and methods

C. elegans genetics

Strain maintenance and genetic manipulations were performed as described(Brenner, 1974). The following strains were used in this study: linkage group (LG) I: *stam-1(ok406)*; LG III: *rabx-5(xd548)*; LG IV: *sand-1(or552)*; LG V: *usp-50(gk632973)*, *usp-50(xd413)*. Mutants and GFP knock-in strains for *rabx-5* are: *xdKi58* (*rabx-5::gfp* knock-in); *xd571* (*rabx-5(K88R)::gfp* knock-in), *xd572* (*rabx-5(K323R)::gfp* knock-in). Additional knock-in strains are: *xdKi22* (*gfp::rab-5* knock-in), *xdKi18* (*gfp::rab-7* knock-in). The reporter strains used in this work are listed as follows: *xdEx2766* (*Psemo-1*::GFP::RAB-5), *xdEx2857* (*Psemo-1*::mCherry::RAB-5), *xdEx2860* (*Psemo-1*::USP-50::GFP), *xdEx2863* (*Psemo-1*::mCherry::RAB-7), *xdEx2991* (*Psemo-1*::USP-50(C492A)::GFP), *xdEx2949* (*Psemo-1*::GFP::SAND-1), *qxIs354* (*Pced-1*::LAAT-1::GFP), *qxIs257* (*Pced-1*::NUC-1::nmCherry), *qxIs352* (*Pced-1*::LAAT-1::nmCherry),

qxIs439 (*Psemo-1*::GFP::TRAM), *qxEx3928* (*Psemo-1*::MANS::GFP), *yqIs75* (*Pvps-29*::VPS-29::GFP), *bIs46 (Pvit-2::GFP::RME-1)*, *opIs334 (Pced-1::YFP::2xFYVE)*, and *Phgrs-1*::HGRS-1::GFP. The CRISPR/Cas9-mediated genome editing strains were generated by Sunny Biotech and were verified with DNA sequencing. All strains were outcrossed with wild type twice before use.

***C. elegans* gene expression constructs**

The complete *usp-50* cDNA was provided by Yuji Kohara (National Institute of Genetics, Japan). The full-length wild-type and C492A mutant *usp-50* cDNAs were cloned into dpSM vector. The P*usp-50,* P*semo-1*, P*myo-3*, and P*vha-6* promoters were cloned into dpSM upstream of the *usp-50* cDNA. The human *usp8* cDNA was cloned into dpSM vector after the P*usp-50* promoter. To express USP-50, SAND-1, RAB-5 or RAB-7 in hyp7, the P*semo-1* promoter was cloned into dpSM vector, followed by GFP, mCherry, or corresponding cDNAs. The full-length and truncated forms of *rabx-5 , sand-1* or *usp-50* cDNAs were cloned into pcDNA3.0 with MYC tag, or pCS2 with 4xFLAG tag. The N-terminus of EEA1 was cloned into pGEX4T-1 vector. All constructs were confirmed by DNA sequencing.

***C. elegans* imaging analysis**

Images of LAAT-1::GFP with NUC-1::mCherry were collected from 3-day-old adults. Images of YFP::2xFYVE with LAAT-1::mCherry were collected from L4 worms. Images were captured by spinning-disk microscopy (Observer Z1; Carl Zeiss). The co-localization analysis was performed with ImageJ software with Pearson correlation coefficient. At least 10 worms were examined. Fluorescence images of worms

expressing LAAT-1::GFP, NUC-1::mCherry at adult day 3 and YFP::2xFYVE, HGRS-1::GFP, GFP::RAB-5 at the L4 stage were captured by spinning-disk microscopy (Observer Z1, Carl Zeiss) in 10-20 z-series (0.3μm/section). A 3D view was reconstituted from the serial optical sections and the number and volume of endosomes and lysosomes were measured using Volocity software (PerkinElmer). At least 10 worms were examined for every genotype at each given developmental stage.

To quantify the fluorescence intensity of USP-50::GFP, RABX-5::GFP, GFP::SAND-1 and GFP::RAB-7, images of strains for comparison were captured with a 63x objective. Mean fluorescence intensity was determined by ImageJ software (National Institute of Health). For line scan analyses, fluorescence intensity values along the solid lines of a given image were extracted with ImageJ software and plotted using Graphpad Prism 8.

***C. elegans* high-pressure freezing electron microscopy**

Young adult worms were cryofixed on a Leica Microsystems HPM 100 and frozen in liquid nitrogen. After high-pressure freezing, the samples were washed four times in acetone and stained with 1% uranyl acetate for 1 hour. The infiltration was performed by increasing the concentration of SPI-PON 812. Samples were placed in fresh resin in an embedding mold and polymerized in 60˚C oven for 3 days. Thin sections (60 nm) were produced with a diamond knife (Diatome) on an ultramicrotome (Ultracut UC7; Leica Microsystems). Sections were pictured with a JEM-1400 TEM (Hitachi HT7700), operating at 80 kV. Pictures were recorded on a Gatan832 4 k × 2.7 k CCD camera. The sizes of vesicles detected in EM were evaluated by NIH ImageJ.

***C. elegans* protein expression and protein-protein interactions**

HEK293T cells were cultured at 37˚C with 5% CO_2 in DMEM supplemented with 10% FBS (Hyclone). Transfections were performed with Lipofectamine 3000 (Invitrogen) according to the manufacturer's instructions. Cultured cells were harvested 24-48 hours after transfection. For immunoprecipitation (IP), whole-cell extracts were collected 24-48 hours after transfection and lysed in RIPA buffer (1% [vol:vol] Triton X-100, 100 mM Tris-HCl, 50 mM EDTA, 150 mM NaCl, 1% deoxycholate, 0.1% SDS with protease inhibitor cocktail (Roche, 04693132001). Worms were lysed with 1% Nonidet P-40 worm lysis buffer (40 mM Tris-HCl, 150 mM NaCl, 1% NP-40) and homogenized with a Dounce homogenizer (Cheng-He Company, Zhuhai, China) on ice for 10 min. Both cell lysates and worm lysates were centrifuged at 12,000 rpm for 15 min at 4˚C and the protein supernatants were incubated with anti-FLAG M2 affinity gel or GFP Nanoab-Agarose. After 8 hours of incubation, the agarose beads were washed with lysis buffer. For protein purification, the immunoprecipitated samples were eluted with 3xFLAG peptide or glycine (pH 2.5) neutralized with Tris buffer (pH 10.4). Immunoprecipitated samples or whole cell lysates were resolved by SDS-PAGE, then transferred to nitrocellulose membranes (Pall Life Sciences). Membranes were blocked with 5% dried milk and signals were visualized with Pierce™ ECL western blotting substrate (Thermo Fisher Scientific, 34095).

***C. elegans* GTP-RAB-5 pull-down assay**

GST or the GST-EEA1-NT fusion protein was expressed in *E. coli* BL21 (DE3) and induced with 0.2 mM IPTG for 12 hours at 25˚C. Bacterial pellets were lysed by

sonication in PBS buffer containing 1% Triton X-100, 1 mM phenylmethylsulphonyl fluoride, and protease inhibitor cocktail. GST or the GST fusion protein was purified using a glutathione Sepharose 4B column (GE Healthcare). GFP::RAB-5 protein from wild-type or *usp-50(xd413)* mutant GFP::RAB-5 KI worms was collected and washed with M9 buffer. Worm lysis buffer containing 1% Nonidet P-40 was then added and samples were disrupted with a Dounce homogenizer on ice for 10 minutes. Debris was removed by centrifuging at 12,000 rpm for 15 minutes at 4˚C. The GFP::RAB-5 input in each experiment was equalized before the pull-down assay. The worm lysates were incubated with GST or GST-EEA1-NT coupled to glutathione Sepharose 4B for 4 hours at 4˚C. After washing five times, the GFP::RAB-5 protein was analyzed by 12% SDS-PAGE followed by standard western blotting with anti-GFP antibody.

***C. elegans* membrane/cytoplasm ratio of GFP::RAB-5**

Images of GFP::RAB-5 KI worms were collected at the L4 stage using spinning-disk microscopy (Observer Z1, Carl Zeiss). The total fluorescence intensity and membranous fluorescence intensity were measured using Volocity software (PerkinElmer). The cytosol fluorescence intensity was measured as total fluorescence intensity minus the membranous fluorescence intensity. Then the membrane/cytoplasm fluorescence intensity ratio was measured. At least 10 worms were examined for each genotype.

***C. elegans* antibodies and reagents**

The primary antibodies used were: anti-GFP (Abcam, ab290), anti-FLAG (Sigma-Aldrich, F1804), anti-tubulin (Sigma-Aldrich, T5168), anti-myc (Santa Cruz

Biotechnology, sc-40). The secondary antibodies used were: goat anti-rabbit IgG-HRP (Santa Cruz Biotechnology, sc-2004) and goat anti-mouse IgG-HRP (Santa Cruz Biotechnology, sc-2005). Anti-FLAG M2 Agarose Affinity Gel (A2220) and 3xFLAG Peptide (F4799) were from Sigma-Aldrich. GFP-Nanoab-Agarose was from Lablead (GNA-50-1000) and Glutathione Sepharose 4B was from GE Healthcare (17075601).

C. elegans statistical analysis

For each western blot, at least three replications were chosen for quantitative analysis with NIH ImageJ following the published protocol (Gallo-Oller et al., 2018). All graphical data are presented as mean ±SEM. Two-tailed unpaired Student's t-tests were performed for comparison between two groups of samples. To compare multiple groups, one-way analysis of variance (ANOVA) followed by Tukey's post-test was performed. The P values are represented as follows: *P< 0.05, **P< 0.01, ***P< 0.001, ****P< 0.0001 and NS (not significant, *P>0.05).

Cell culture

The human breast cancer SUM159 cells, kindly provided by J. Brugge (Harvard Medical School, Boston, MA), were confirmed by STR genotyping and verified to be mycoplasma-free using the TransDetect PCR Mycoplasma Detection Kit (TransGen Biotech). SUM159 cells were cultured at 37˚C and 5% CO_2 in DMEM/F-12 (Corning), supplemented with 5% FBS (Gibco), 100 U/ml penicillin, streptomycin (Corning), 1 μg/ml hydrocortisone (Sigma-Aldrich), 5 μg/ml insulin (Sigma-Aldrich), and 20 mM HEPES (Corning), pH 7.4.

Plasmids and transfection

The cDNA sequence of human Rabex5 was amplified from SUM159 cDNA and inserted into a vector containing mEGFP or mScarlet-I to generate the plasmids Rabex5-mEGFP and Rabex5-mScarlet-I using the Gibson assembly method (pEASY-Uni Seamless Cloning and Assembly Kit, TransGen Biotech). The cDNA sequences of human Rab7a, Lamp1, EEA1, Rab5c were amplified from the related cDNA clones and inserted into the mScarlet-I-, mEGFP-, or Halo-containing vectors to generate the plasmids mScarlet-I-Rab7A, Lamp1-mScarlet-I, mScarlet-I-EEA1, mScarlet-I-Rab5c, mEGFP-Rab5c, or Halo-Rab5c using the Gibson assembly method. Transfections were performed using Lipofectamine 3000 Transfection Reagent (Invitrogen) according to the manufacturer's instructions. Cells expressing fluorescently-tagged proteins at relatively low levels were imaged 16–20 hours after transfection.

Genome editing of SUM159 cells to generate mEGFP-USP8$^{+/+}$, mEGFP-Mon1a$^{+/+}$ or mEGFP-Mon1b$^{+/+}$ cells using the CRISPR/Cas9 approach

SUM159 cells were genome-edited to incorporate mEGFP at the N-terminus of USP8, Mon1a, and Mon1b using the CRISPR/Cas9 approach as described (He et al., 2017; Ran et al., 2013). The single-guide RNAs (sgRNA) targeting human USP8 (5'-ATGCAGATTAGATCGTGATG-3'), human Mon1a (5'-GGATGGCTACTGACATGCAG-3'), or human Mon1b (5'-GATGTGCAGATGGAGGTCGG-3') were cloned into pSpCas9(BB)-2A-Puro (PX459) (Addgene #48139). The donor constructs used for homologous recombination were generated by cloning into the pUC19 vector with two ~600-800-nucleotide fragments of genomic DNA upstream and downstream of the start codon of human

USP8, Mon1a, and Mon1b, and the open reading frame of mEGFP using the pEASY-Uni Seamless Cloning and Assembly Kit (TransGen Biotech). A flexible $(GGS)_3$ linker was inserted between the start or stop codon of the gene and the open reading frame of mEGFP. 4-5 days after transfection with the donor plasmid and PX459 plasmid containing sgRNA targeting sequence, SUM159 cells expressing mEGFP were enriched by fluorescence-activated cell sorting (FACSAria Fusion, BD Biosciences). The sorted positive cells were expanded and then subjected to single-cell sorting into 96-well plates. The genome-edited monoclonal cell populations were identified by PCR (GoTaq Polymerase, Promega) and then verified by western blot analysis and imaging.

Genome editing of SUM159 cells to generate CLTA-miRFP670nano$^{+/+}$ cells using the TALEN-based approach

SUM159 cells were genome-edited to incorporate miRFP670nano into the C terminus of clathrin light chain A (CLTA) using a TALEN-based protocol as described (He et al., 2017; Ran et al., 2013). SUM159 cells were transfected with 800 ng each of the upstream and downstream TALEN targeting sequences and the donor construct using Lipofectamine 3000 (Invitrogen) according to the manufacturer's instructions. The monoclonal cell line with both alleles edited for CLTA-miRFP670nano was generated as described above.

Knockout of USP8 using the CRISPR/Cas9 approach

Knockout of USP8 in SUM159 cells was performed using the CRISPR/Cas9 approach as described (He et al., 2017; Ran et al., 2013). The sgRNA targeting the human USP8 gene (5'-ATGCAGATTAGATCGTGATG-3') was cloned into pSpCas9(BB)-2A-Halo.

pSpCas9(BB)-2A-Halo was generated by replacing GFP with HaloTag in pSpCas9(BB)-2A-GFP (PX458) (Addgene #488138). SUM159 cells were transfected with 1000 ng of the plasmid containing the sgRNA targeting sequence using Lipofectamine 3000. 24 hours after transfection, the cells expressing HaloTag were subjected to single-cell sorting into 96-well plates (FACSAria Fusion, BD Biosciences). The monoclonal cell populations with frameshift deletions in both alleles of *USP8* were identified by sequencing and confirmed by western blot analysis.

Knock-down of USP8 expression by siRNA

The siRNA (GenePharma) used to knock down the expression of USP8 was transfected into cells by using Lipofectamine RNAiMAX (Invitrogen) according to the manufacturer's instructions. The siRNA sequence targeting human *USP8* was 5'-CCAAAGAGAAAGGAGCAAT-3'(Jing et al., 2020). The non-targeting siRNA mixture (5'-ATGTATTGGCCTGTATTAG-3', 5'-GCGACGATCTGCCTAAGAT-3', and 5'-TTTCCGCACTGTGATTCGG-3') was used as a control. Knock-down of USP8 by siRNA was achieved by two sequential transfections on day 1 and day 3 (cells plated on day 0), followed by analysis on day 5.

Live-cell imaging by spinning-disk confocal microscopy and imaging analysis

The spinning-disk confocal microscope was built on the Nikon TiE microscope as described (Bi et al., 2021). Briefly, the microscope was equipped with a CFI Apochromat SD 100X objective (1.46 NA, Nikon), a Motorized XY stage (Prior Scientific), a fully enclosed and environmentally controlled cage incubator (Okolab), OBIS 488, 561 and 647 nm lasers (Coherent), a CSU-X1 spinning-disk confocal unit

(Yokogawa) and an EMCCD camera (iXon Ultra 897, Andor Technology). Images were acquired using Micro-Manager 2.0 (Edelstein et al., 2010).

SUM159 cells were plated on single-well confocal dishes (Cellvis) approximately 6-8 hours after transfection. Cells expressing relatively low levels of the endosome makers were imaged from the bottom surface (Z = 1) to the middle plane (spaced 0.35 μm) in phenol-free DMEM/F12 (Corning) containing 5% FBS and 20 mM HEPES. Single frames or merge images were generated in Fiji (Schindelin et al., 2012). To quantify the areas and numbers of the fluorescently labeled Rab5c, Rabex5, or EEA1 spots per cell, the cell boundary was firstly manually segmented based on the fluorescence of the cell in Fiji (Schindelin et al., 2012). The raw image and the segmented cell boundary were then loaded into Cellprofiler 4 (Stirling et al., 2021) (http://www.cellprofiler.org) to detect the numbers and areas of spots in the middle plane of the cell (optical section Z = 4). Finally, these results were exported from Cellprofiler 4 and further analyzed and plotted using GraphPad Prism 9.

For live-cell imaging and tracking of USP8 recruitment to Rab5-positive carriers, USP8-mEGFP$^{+/+}$ cells were transiently transfected with mScarlet-I-Rab5c, and then imaged at two planes (the bottom plane and the plane 0.5 μm above the bottom plane) every 2 seconds for 60 seconds by spinning-disk confocal microscopy. The maximum fluorescence intensity projection of the two imaging planes was generated using Fiji and was used for further imaging analysis. The detection and tracking of Rab5-positive carriers in the time-lapse series were performed using the TrackMate 7 plugin in Fiji (Ershov et al., 2022; Tinevez et al., 2017). The mScarlet-I-Rab5c channel was used for

spot detection and tracking. Then the fluorescence intensities of mScarlet-I-Rab5c and USP8-mEGFP were extracted and plotted. Montages were generated using the Multi Kymograph plugin in Fiji.

Imaging by SIM

Imaging of the sub-organelle distribution of USP8 on EEs was performed on the multi-SIM system as described (Qiao et al., 2022). The mEGFP-USP8$^{+/+}$ cells transiently expressed relatively low levels of mScarlet-I-EEA1 and the images were acquired with a CFI SR HP Apo TIRF 100X objective (1.49 NA, Nikon) and a sCMOS camera (Kinetix, TELEDYNE PHOTOMETRICS).

Western blot analysis

SUM159 cells were lysed at 4˚C for 20 minutes with RIPA lysis buffer (Sigma-Aldrich) containing a protease inhibitor cocktail (Thermo Scientific), and then pelleted at 12,000 g for 15 minutes at 4˚C. The supernatant was mixed with 5× sample buffer (MB01015, GenScript), heated to 100˚C for 8-10 minutes, and then fractionated by SDS–PAGE (TGX FastCast AcrylamideKit, 10%, Bio-Rad) and transferred to nitrocellulose membranes (PALL). The membranes were incubated in TBST buffer containing 5% skim milk for 1 hour at room temperature, followed by overnight incubation at 4˚C with the specific primary antibodies. After three washes in TBST (5 min each), the membranes were incubated with the appropriate HRP-conjugated secondary antibody (Beyotime, 1:1,000) at room temperature for 1 hour. The membrane was incubated with the SignalFire™ ECL Reagent (Cell Signaling) or BeyoECL Moon (Beyotime) and imaged by the Tanon-5200 Chemiluminescent Imaging System (Tanon). The primary antibodies used in this study were: USP8 (sc-376130, 1:500, Santa Cruz), GFP (14-6674-82, 1:1,000, Invitrogen), EEA1 (610456, 1:1,000, BD Biosciences), GAPDH

(60004-1-Ig, 1:50,000, Proteintech).

Immunofluorescence

For immunofluorescence staining, cells were cultured on small coverslips (801010, NEST) coated with PDL. Cells were washed with PBS once, and then fixed using 4% PFA (157-8, Electron Microscopy Sciences) for 20 minutes at room temperature. After washing with PBS for three times, the samples were incubated with 0.5% Triton X-100 in PBS for 15 minutes at room temperature. Then the samples were incubated in the blocking buffer (1% BSA in PBS) for 60 minutes at room temperature. Afterwards, the samples were incubated with the primary antibody against EEA1 (1:200 in 1% BSA) overnight at 4˚C. After washing with PBS for five times, the samples were incubated with the Alexa Fluor 488- or 555-conjugated secondary antibodies (1:500 in 1% BSA, Thermo Fisher) for 60 minutes at room temperature. After washing with PBS for five times and ddH_2O once, the coverslip was mounted on a slide with the FluorSave™ Reagent (Merck, 345789-20ML). The prepared samples were imaged by the spinning-disk confocal microscope described above.

Acknowledgments

We thank Drs. Xiaochen Wang, Chonglin Yang, Qi Xie, Hong Zhang, Yuji Kohara, Xun Huang, Luke D. Lavis, Tom Kirchhausen, Joan Brugge, the Million Mutation Project, and the Caenorhabditis Genetics Center for providing reagents, strains, and technical support. This work was supported by the National Key R&D Program of China (2021YFA0805802 to M.D. and 2022YFA1304500 and 2021YFA0804802 to K.H.) and

the National Natural Science Foundation of China (32070810 and 31921002 to M.D. and 32321004 and 92354305 to K.H.).

References

Abenza, J.F., A. Galindo, A. Pantazopoulou, C. Gil, V. de los Rios, and M.A. Penalva. 2010. Aspergillus RabB Rab5 integrates acquisition of degradative identity with the long distance movement of early endosomes. *Mol. Biol. Cell*. 21:2756-2769. https://doi.org/10.1091/mbc.e10-02-0119

Adoro, S., K.H. Park, S.E. Bettigole, R. Lis, H.R. Shin, H. Seo, J.H. Kim, K.P. Knobeloch, J.H. Shim, and L.H. Glimcher. 2017. Post-translational control of T cell development by the ESCRT protein CHMP5. *Nat. Immunol.* 18:780-790. http://doi.org/10.1038/ni.3764

Ali, N., L. Zhang, S. Taylor, A. Mironov, S. Urbé, and P. Woodman. 2013. Recruitment of UBPY and ESCRT exchange drive HD-PTP-dependent sorting of EGFR to the MVB. *Curr. Biol.* 23:453-461. http://doi.org/10.1016/j.cub.2013.02.033

Alwan, H.A., and J.E. van Leeuwen. 2007. UBPY-mediated epidermal growth factor receptor (EGFR) de-ubiquitination promotes EGFR degradation. *J. Biol. Chem.* 282:1658-1669. http://doi.org/10.1074/jbc.M604711200

Babst, M. 2011. MVB vesicle formation: ESCRT-dependent, ESCRT-independent and everything in between. *Curr. Opin. Cell Biol.* 23:452-457. http://doi.org/10.1016/j.ceb.2011.04.008

Balderhaar, H.J., J. Lachmann, E. Yavavli, C. Bröcker, A. Lürick, and C. Ungermann. 2013. The CORVET complex promotes tethering and fusion of Rab5/Vps21-positive membranes. *Proc. Natl. Acad. Sci. USA*. 110:3823-3828. http://doi.org/10.1073/pnas.1221785110

Berlin, I., K.M. Higginbotham, R.S. Dise, M.I. Sierra, and P.D. Nash. 2010a. The deubiquitinating enzyme USP8 promotes trafficking and degradation of the chemokine receptor 4 at the sorting endosome. *J. Biol. Chem.* 285:37895-37908. http://doi.org/10.1074/jbc.M110.129411

Berlin, I., H. Schwartz, and P.D. Nash. 2010b. Regulation of epidermal growth factor receptor ubiquitination and trafficking by the USP8·STAM complex. *J. Biol. Chem.* 285:34909-34921. http://doi.org/10.1074/jbc.M109.016287

Bi, G., M. Su, N. Li, Y. Liang, S. Dang, J. Xu, M. Hu, J. Wang, M. Zou, Y. Deng, Q. Li, S. Huang, J. Li, J. Chai, K. He, Y.H. Chen, and J.M. Zhou. 2021. The ZAR1 resistosome is a calcium-permeable channel triggering plant immune signaling. *Cell*. 184:3528-3541.e3512. http://doi.org/10.1016/j.cell.2021.05.003

Borchers, A.C., M. Janz, J.H. Schäfer, A. Moeller, D. Kümmel, A. Paululat, C. Ungermann, and L. Langemeyer. 2023. Regulatory sites in the Mon1-Ccz1 complex control Rab5 to Rab7 transition and endosome maturation. *Proc. Natl. Acad. Sci. USA*. 120:e2303750120. http://doi.org/10.1073/pnas.2303750120

Borchers, A.C., L. Langemeyer, and C. Ungermann. 2021. Who's in control? Principles of Rab GTPase activation in endolysosomal membrane trafficking and beyond. *J. Cell Biol.* 220:e202105120. http://doi.org/10.1083/jcb.202105120

Bowers, K., J. Lottridge, S.B. Helliwell, L.M. Goldthwaite, J.P. Luzio, and T.H. Stevens. 2004. Protein-protein interactions of ESCRT complexes in the yeast *Saccharomyces cerevisiae*. *Traffic*. 5:194-

210. http://doi.org/10.1111/j.1600-0854.2004.00169.x

Bowers, K., S.C. Piper, M.A. Edeling, S.R. Gray, D.J. Owen, P.J. Lehner, and J.P. Luzio. 2006. Degradation of endocytosed epidermal growth factor and virally ubiquitinated major histocompatibility complex class I is independent of mammalian ESCRTII. *J. Biol. Chem.* 281:5094-5105. https://doi.org/10.1074/jbc.M508632200

Brenner, S. 1974. The genetics of *Caenorhabditis elegans*. *Genetics*. 77:71-94. https://doi.org/10.1093/genetics/77.1.71

Byun, S., S.Y. Lee, J. Lee, C.H. Jeong, L. Farrand, S. Lim, K. Reddy, J.Y. Kim, M.H. Lee, H.J. Lee, A.M. Bode, K. Won Lee, and Z. Dong. 2013. USP8 is a novel target for overcoming gefitinib resistance in lung cancer. *Clin. Cancer Res.* 19:3894-3904. http://doi.org/10.1158/1078-0432.ccr-12-3696

Christoforidis, S., H.M. McBride, R.D. Burgoyne, and M. Zerial. 1999. The Rab5 effector EEA1 is a core component of endosome docking. *Nature*. 397:621-625. https://doi.org/10.1038/17618

Crespo-Yàñez, X., C. Aguilar-Gurrieri, A.C. Jacomin, A. Journet, M. Mortier, E. Taillebourg, E. Soleilhac, W. Weissenhorn, and M.O. Fauvarque. 2018. CHMP1B is a target of USP8/UBPY regulated by ubiquitin during endocytosis. *PLoS Genet.* 14:e1007456. http://doi.org/10.1371/journal.pgen.1007456

Dehnen, L., M. Janz, J.K. Verma, O.E. Psathaki, L. Langemeyer, F. Fröhlich, J.J. Heinisch, H. Meyer, C. Ungermann, and A. Paululat. 2020. A trimeric metazoan Rab7 GEF complex is crucial for endocytosis and scavenger function. *J. Cell Sci.* 133. https://doi.org/10.1242/jcs.247080

Delprato, A., and D.G. Lambright. 2007. Structural basis for Rab GTPase activation by VPS9 domain exchange factors. *Nat. Struct. Mol. Biol.* 14:406-412. http://doi.org/10.1038/nsmb1232

Dickinson, D.J., J.D. Ward, D.J. Reiner, and B. Goldstein. 2013. Engineering the Caenorhabditis elegans genome using Cas9-triggered homologous recombination. *Nat. Methods*. 10:1028-1034. https://doi.org/10.1038/nmeth.2641

Dufner, A., and K.P. Knobeloch. 2019. Ubiquitin-specific protease 8 (USP8/UBPy): a prototypic multidomain deubiquitinating enzyme with pleiotropic functions. *Biochem. Soc. Trans.* 47:1867-1879. http://doi.org/10.1042/BST20190527

Edelstein, A., N. Amodaj, K. Hoover, R. Vale, and N. Stuurman. 2010. Computer control of microscopes using µManager. *Curr. Protoc. Mol. Biol.* Chapter 14:Unit14.20. http://doi.org/10.1002/0471142727.mb1420s92

Ershov, D., M.S. Phan, J.W. Pylvänäinen, S.U. Rigaud, L. Le Blanc, A. Charles-Orszag, J.R.W. Conway, R.F. Laine, N.H. Roy, D. Bonazzi, G. Duménil, G. Jacquemet, and J.Y. Tinevez. 2022. TrackMate 7: integrating state-of-the-art segmentation algorithms into tracking pipelines. *Nat. Methods*. 19:829-832. https://doi.org/10.1038/s41592-022-01507-1

Gallo-Oller, G., R. Ordoñez, and J. Dotor. 2018. A new background subtraction method for Western blot densitometry band quantification through image analysis software. *J. Immunol. Methods*. 457:1-5. http://doi.org/10.1016/j.jim.2018.03.004

Gao, J., L. Langemeyer, D. Kümmel, F. Reggiori, and C. Ungermann. 2018. Molecular mechanism to target the endosomal Mon1-Ccz1 GEF complex to the pre-autophagosomal structure. *eLife*. 7:e31145. https://doi.org/10.7554/eLife.31145

He, K., R. Marsland, III, S. Upadhyayula, E. Song, S. Dang, B.R. Capraro, W. Wang, W. Skillern, R. Gaudin, M. Ma, and T. Kirchhausen. 2017. Dynamics of phosphoinositide conversion in clathrin-mediated endocytic traffic. *Nature*. 552:410-414. https://doi.org/10.1038/nature25146

Hiragi, S., T. Matsui, Y. Sakamaki, and M. Fukuda. 2022. TBC1D18 is a Rab5-GAP that coordinates

endosome maturation together with Mon1. *J. Cell Biol.* 221:e202201114. https://doi.org/10.1083/jcb.202201114

Horiuchi, H., R. Lippé, H.M. McBride, M. Rubino, P. Woodman, H. Stenmark, V. Rybin, M. Wilm, K. Ashman, M. Mann, and M. Zerial. 1997. A novel Rab5 GDP/GTP exchange factor complexed to Rabaptin-5 links nucleotide exchange to effector recruitment and function. *Cell*. 90:1149-1159. https://doi.org/10.1016/s0092-8674(00)80380-3

Huotari, J., and A. Helenius. 2011. Endosome maturation. *EMBO J.* 30:3481-3500. https://doi.org/10.1038/emboj.2011.286

Huynh, J.M., H. Dang, I.A. Munoz-Tucker, M. O'Ketch, I.T. Liu, S. Perno, N. Bhuyan, A. Crain, I. Borbon, and H. Fares. 2016. ESCRT-dependent cell death in a *Caenorhabditis elegans* model of the lysosomal storage disorder mucolipidosis type IV. *Genetics*. 202:619-638. https://doi.org/10.1534/genetics.115.182485

Islam, M.T., F. Chen, and H. Chen. 2021. The oncogenic role of ubiquitin specific peptidase (USP8) and its signaling pathways targeting for cancer therapeutics. *Arch. Biochem. Biophys.* 701:108811. http://doi.org/10.1016/j.abb.2021.108811

Jacomin, A.C., A. Bescond, E. Soleilhac, B. Gallet, G. Schoehn, M.O. Fauvarque, and E. Taillebourg. 2015. The deubiquitinating enzyme UBPY is required for lysosomal biogenesis and productive autophagy in *Drosophila*. *PLoS One*. 10:e0143078. https://doi.org/10.1371/journal.pone.0143078

Jacomin, A.C., M.O. Fauvarque, and E. Taillebourg. 2016. A functional endosomal pathway is necessary for lysosome biogenesis in Drosophila. *BMC Cell Biol.* 17:36. http://doi.org/10.1186/s12860-016-0115-7

Jing, X., Y. Chen, Y. Chen, G. Shi, S. Lv, N. Cheng, C. Feng, Z. Xin, L. Zhang, and J. Wu. 2020. Down-regulation of USP8 Inhibits Cholangiocarcinoma Cell Proliferation and Invasion. *Cancer Manag. Res.* 12:2185-2194. http://doi.org/10.2147/cmar.s234586

Kato, M., K. Miyazawa, and N. Kitamura. 2000. A deubiquitinating enzyme UBPY interacts with the Src homology 3 domain of Hrs-binding protein via a novel binding motif PX(V/I)(D/N)RXXKP. *J. Biol. Chem.* 275:37481-37487. http://doi.org/10.1074/jbc.M007251200

Komander, D., M.J. Clague, and S. Urbé. 2009. Breaking the chains: structure and function of the deubiquitinases. *Nat. Rev. Mol. Cell Biol.* 10:550-563. https://doi.org/10.1038/nrm2731

Kümmel, D., E. Herrmann, L. Langemeyer, and C. Ungermann. 2023. Molecular insights into endolysosomal microcompartment formation and maintenance. *Biol. Chem.* 404:441-454. https://doi.org/10.1515/hsz-2022-0294

Langemeyer, L., A.C. Borchers, E. Herrmann, N. Füllbrunn, Y. Han, A. Perz, K. Auffarth, D. Kümmel, and C. Ungermann. 2020. A conserved and regulated mechanism drives endosomal Rab transition. *eLife*. 9:e56090. https://doi.org/10.7554/eLife.56090

Lauer, J., S. Segeletz, A. Cezanne, G. Guaitoli, F. Raimondi, M. Gentzel, V. Alva, M. Habeck, Y. Kalaidzidis, M. Ueffing, A.N. Lupas, C.J. Gloeckner, and M. Zerial. 2019. Auto-regulation of Rab5 GEF activity in Rabex5 by allosteric structural changes, catalytic core dynamics and ubiquitin binding. *eLife*. 8:e46302. https://doi.org/10.7554/eLife.46302

Lawe, D.C., A. Chawla, E. Merithew, J. Dumas, W. Carrington, K. Fogarty, L. Lifshitz, R. Tuft, D. Lambright, and S. Corvera. 2002. Sequential Roles for Phosphatidylinositol 3-Phosphate and Rab5 in Tethering and Fusion of Early Endosomes via Their Interaction with EEA1. *J. Biol. Chem.* 277:8611-8617. https://doi.org/10.1074/jbc.M109239200

Li, H., Y. Sun, Y. Yao, S. Ke, N. Zhang, W. Xiong, J. Shi, C. He, X. Xiao, H. Yu, P. Dai, B. Xiang, X. Xing, G. Xu, W. Song, J. Song, and J. Zhang. 2024. USP8-governed GPX4 homeostasis orchestrates ferroptosis and cancer immunotherapy. *Proc Natl Acad Sci U S A*. 121:e2315541121. http://doi.org/10.1073/pnas.2315541121

Lippé, R., M. Miaczynska, V. Rybin, A. Runge, and M. Zerial. 2001. Functional synergy between Rab5 effector Rabaptin-5 and exchange factor Rabex-5 when physically associated in a complex. *Mol. Biol. Cell*. 12:2219-2228. https://doi.org/10.1091/mbc.12.7.2219

Liu, B., H.W. Du, R. Rutkowski, A. Gartner, and X.C. Wang. 2012. LAAT-1 is the lysosomal lysine/arginine transporter that maintains amino acid homeostasis. *Science*. 337:351-354. https://doi.org/10.1126/science.1220281

Ma, Z.Y., Z.J. Song, J.H. Chen, Y.F. Wang, S.Q. Li, L.F. Zhou, Y. Mao, Y.M. Li, R.G. Hu, Z.Y. Zhang, H.Y. Ye, M. Shen, X.F. Shou, Z.Q. Li, H. Peng, Q.Z. Wang, D.Z. Zhou, X.L. Qin, J. Ji, J. Zheng, H. Chen, Y. Wang, D.Y. Geng, W.J. Tang, C.W. Fu, Z.F. Shi, Y.C. Zhang, Z. Ye, W.Q. He, Q.L. Zhang, Q.S. Tang, R. Xie, J.W. Shen, Z.J. Wen, J. Zhou, T. Wang, S. Huang, H.J. Qiu, N.D. Qiao, Y. Zhang, L. Pan, W.M. Bao, Y.C. Liu, C.X. Huang, Y.Y. Shi, and Y. Zhao. 2015. Recurrent gain-of-function USP8 mutations in Cushing's disease. *Cell Res.* 25:306-317. http://doi.org/10.1038/cr.2015.20

MacDonald, E., S. Urbé, and M.J. Clague. 2014. USP8 controls the trafficking and sorting of lysosomal enzymes. *Traffic*. 15:879-888. https://doi.org/10.1111/tra.12180

Martín-Rodríguez, C., M. Song, B. Anta, F.J. González-Calvo, R. Deogracias, D. Jing, F.S. Lee, and J.C. Arevalo. 2020. TrkB deubiquitylation by USP8 regulates receptor levels and BDNF-dependent neuronal differentiation. *J. Cell Sci.* 133:jcs247841. https://doi.org/10.1242/jcs.247841

Mathieu, J., P. Michel-Hissier, V. Boucherit, and J.R. Huynh. 2022. The deubiquitinase USP8 targets ESCRT-III to promote incomplete cell division. *Science*. 376:818-823. https://doi.org/10.1126/science.abg2653

Mattera, R., and J.S. Bonifacino. 2008. Ubiquitin binding and conjugation regulate the recruitment of Rabex-5 to early endosomes. *EMBO J.* 27:2484-2494. https://doi.org/10.1038/emboj.2008.177

Mizuno, E., T. Iura, A. Mukai, T. Yoshimori, N. Kitamura, and M. Komada. 2005. Regulation of epidermal growth factor receptor down-regulation by UBPY-mediated deubiquitination at endosomes. *Mol. Biol. Cell*. 16:5163-5174. http://doi.org/10.1091/mbc.e05-06-0560

Mizuno, E., K. Kobayashi, A. Yamamoto, N. Kitamura, and M. Komada. 2006. A deubiquitinating enzyme UBPY regulates the level of protein ubiquitination on endosomes. *Traffic*. 7:1017-1031. https://doi.org/10.1111/j.1600-0854.2006.00452.x

Naviglio, S., C. Mattecucci, B. Matoskova, T. Nagase, N. Nomura, P.P. Di Fiore, and G.F. Draetta. 1998. UBPY: a growth-regulated human ubiquitin isopeptidase. *EMBO J.* 17:3241-3250. http://doi.org/10.1093/emboj/17.12.3241

Niendorf, S., A. Oksche, A. Kisser, J. Lohler, M. Prinz, H. Schorle, S. Feller, M. Lewitzky, I. Horak, and K.P. Knobeloch. 2007. Essential role of ubiquitin-specific protease 8 for receptor tyrosine kinase stability and endocytic trafficking in vivo. *Mol. Cell Biol.* 27:5029-5039. http://doi.org/10.1128/MCB.01566-06

Nordmann, M., M. Cabrera, A. Perz, C. Bröcker, C. Ostrowicz, S. Engelbrecht-Vandré, and C. Ungermann. 2010. The Mon1-Ccz1 complex is the GEF of the late endosomal Rab7 homolog Ypt7. *Curr. Biol.* 20:1654-1659. http://doi.org/10.1016/j.cub.2010.08.002

Ohya, T., M. Miaczynska, U. Coskun, B. Lommer, A. Runge, D. Drechsel, Y. Kalaidzidis, and M. Zerial. 2009.

Reconstitution of Rab- and SNARE-dependent membrane fusion by synthetic endosomes. *Nature*. 459:1091-1097. https://doi.org/10.1038/nature08107

Peng, H., F. Yang, Q. Hu, J. Sun, C. Peng, Y. Zhao, and C. Huang. 2020. The ubiquitin-specific protease USP8 directly deubiquitinates SQSTM1/p62 to suppress its autophagic activity. *Autophagy*. 16:698-708. http://doi.org/10.1080/15548627.2019.1635381

Peplowska, K., D.F. Markgraf, C.W. Ostrowicz, G. Bange, and C. Ungermann. 2007. The CORVET tethering complex interacts with the yeast Rab5 homolog Vps21 and is involved in endo-lysosomal biogenesis. *Dev. Cell*. 12:739-750. http://doi.org/10.1016/j.devcel.2007.03.006

Poteryaev, D., S. Datta, K. Ackema, M. Zerial, and A. Spang. 2010. Identification of the switch in early-to-late endosome transition. *Cell*. 141:497-508. https://doi.org/10.1016/j.cell.2010.03.011

Qiao, C., D. Li, Y. Liu, S. Zhang, K. Liu, C. Liu, Y. Guo, T. Jiang, C. Fang, N. Li, Y. Zeng, K. He, X. Zhu, J. Lippincott-Schwartz, Q. Dai, and D. Li. 2022. Rationalized deep learning super-resolution microscopy for sustained live imaging of rapid subcellular processes. *Nat. Biotechnol.* https://doi.org/10.1038/s41587-022-01471-3

Ran, F.A., P.D. Hsu, J. Wright, V. Agarwala, D.A. Scott, and F. Zhang. 2013. Genome engineering using the CRISPR-Cas9 system. *Nat. Protoc.* 8:2281-2308. https://doi.org/10.1038/nprot.2013.143

Reincke, M., S. Sbiera, A. Hayakawa, M. Theodoropoulou, A. Osswald, F. Beuschlein, T. Meitinger, E. Mizuno-Yamasaki, K. Kawaguchi, Y. Saeki, K. Tanaka, T. Wieland, E. Graf, W. Saeger, C.L. Ronchi, B. Allolio, M. Buchfelder, T.M. Strom, M. Fassnacht, and M. Komada. 2015. Mutations in the deubiquitinase gene USP8 cause Cushing's disease. *Nat. Genet.* 47:31-38. http://doi.org/10.1038/ng.3166

Row, P.E., H. Liu, S. Hayes, R. Welchman, P. Charalabous, K. Hofmann, M.J. Clague, C.M. Sanderson, and S. Urbé. 2007. The MIT domain of UBPY constitutes a CHMP binding and endosomal localization signal required for efficient epidermal growth factor receptor degradation. *J. Biol. Chem.* 282:30929-30937. http://doi.org/10.1074/jbc.M704009200

Row, P.E., I.A. Prior, J. McCullough, M.J. Clague, and S. Urbe. 2006. The ubiquitin isopeptidase UBPY regulates endosomal ubiquitin dynamics and is essential for receptor down-regulation. *J. Biol. Chem.* 281:12618-12624. http://doi.org/10.1074/jbc.M512615200

Sardana, R., and S.D. Emr. 2021. Membrane Protein Quality Control Mechanisms in the Endo-Lysosome System. *Trends Cell Biol.* 31:269-283. https://doi.org/10.1016/j.tcb.2020.11.011

Schindelin, J., I. Arganda-Carreras, E. Frise, V. Kaynig, M. Longair, T. Pietzsch, S. Preibisch, C. Rueden, S. Saalfeld, B. Schmid, J.Y. Tinevez, D.J. White, V. Hartenstein, K. Eliceiri, P. Tomancak, and A. Cardona. 2012. Fiji: an open-source platform for biological-image analysis. *Nat. Methods*. 9:676-682. http://doi.org/10.1038/nmeth.2019

Stenmark, H. 2009. Rab GTPases as coordinators of vesicle traffic. *Nat. Rev. Mol. Cell Biol.* 10:513-525. http://doi.org/10.1038/nrm2728

Stenmark, H., R. Aasland, B.-H. Toh, and A. D'Arrigo. 1996. Endosomal Localization of the Autoantigen EEA1 Is Mediated by a Zinc-binding FYVE Finger. *J. Biol. Chem.* 271:24048-24054. https://doi.org/10.1074/jbc.271.39.24048

Stenmark, H., R.G. Parton, O. Steele-Mortimer, A. Lutcke, J. Gruenberg, and M. Zerial. 1994. Inhibition of rab5 GTPase activity stimulates membrane fusion in endocytosis. *EMBO J.* 13:1287-1296. https://doi.org/10.1002/j.1460-2075.1994.tb06381.x

Stirling, D.R., M.J. Swain-Bowden, A.M. Lucas, A.E. Carpenter, B.A. Cimini, and A. Goodman. 2021. CellProfiler 4: improvements in speed, utility and usability. *BMC Bioinformatics*. 22:433.

https://doi.org/10.1186/s12859-021-04344-9

Stuffers, S., C. Sem Wegner, H. Stenmark, and A. Brech. 2009. Multivesicular endosome biogenesis in the absence of ESCRTs. *Traffic*. 10:925-937. https://doi.org/10.1111/j.1600-0854.2009.00920.x

Sun, J., Q. Hu, H. Peng, C. Peng, L. Zhou, J. Lu, and C. Huang. 2018. The ubiquitin-specific protease USP8 deubiquitinates and stabilizes Cx43. *J. Biol. Chem.* 293:8275-8284. http://doi.org/10.1074/jbc.RA117.001315

Sun, Y., M. Li, D. Zhao, X. Li, C. Yang, and X. Wang. 2020. Lysosome activity is modulated by multiple longevity pathways and is important for lifespan extension in *C. elegans*. *eLife*. 9:e55745. https://doi.org/10.7554/eLife.55745

Theos, A.C., S.T. Truschel, D. Tenza, I. Hurbain, D.C. Harper, J.F. Berson, P.C. Thomas, G. Raposo, and M.S. Marks. 2006. A lumenal domain-dependent pathway for sorting to intralumenal vesicles of multivesicular endosomes involved in organelle morphogenesis. *Dev. Cell*. 10:343-354. https://doi.org/10.1016/j.devcel.2006.01.012

Tinevez, J.Y., N. Perry, J. Schindelin, G.M. Hoopes, G.D. Reynolds, E. Laplantine, S.Y. Bednarek, S.L. Shorte, and K.W. Eliceiri. 2017. TrackMate: An open and extensible platform for single-particle tracking. *Methods*. 115:80-90. https://doi.org/10.1016/j.ymeth.2016.09.016

Tremel, S., Y. Ohashi, D.R. Morado, J. Bertram, O. Perisic, L.T.L. Brandt, M.K. von Wrisberg, Z.A. Chen, S.L. Maslen, O. Kovtun, M. Skehel, J. Rappsilber, K. Lang, S. Munro, J.A.G. Briggs, and R.L. Williams. 2021. Structural basis for VPS34 kinase activation by Rab1 and Rab5 on membranes. *Nat. Commun.* 12:1564. https://doi.org/10.1038/s41467-021-21695-2

Vaites, L.P., J.A. Paulo, E.L. Huttlin, and J.W. Harper. 2018. Systematic Analysis of Human Cells Lacking ATG8 Proteins Uncovers Roles for GABARAPs and the CCZ1/MON1 Regulator C18orf8/RMC1 in Macroautophagic and Selective Autophagic Flux. *Mol. Cell Biol.* 38. https://doi.org/10.1128/mcb.00392-17

van den Boomen, D.J.H., A. Sienkiewicz, I. Berlin, M.L.M. Jongsma, D.M. van Elsland, J.P. Luzio, J.J.C. Neefjes, and P.J. Lehner. 2020. A trimeric Rab7 GEF controls NPC1-dependent lysosomal cholesterol export. *Nat. Commun.* 11:5559. https://doi.org/10.1038/s41467-020-19032-0

Wang, C.W., P.E. Stromhaug, J. Shima, and D.J. Klionsky. 2002. The Ccz1-Mon1 protein complex is required for the late step of multiple vacuole delivery pathways. *J. Biol. Chem.* 277:47917-47927. https://doi.org/10.1074/jbc.M208191200

Wegner, C.S., L. Malerod, N.M. Pedersen, C. Progida, O. Bakke, H. Stenmark, and A. Brech. 2010. Ultrastructural characterization of giant endosomes induced by GTPase-deficient Rab5. *Histochem. Cell Biol.* 133:41-55. http://doi.org/10.1007/s00418-009-0643-8

Wollert, T., and J.H. Hurley. 2010. Molecular mechanism of multivesicular body biogenesis by ESCRT complexes. *Nature*. 464:864-869. https://doi.org/10.1038/nature08849

Wright, M.H., I. Berlin, and P.D. Nash. 2011. Regulation of endocytic sorting by ESCRT-DUB-mediated deubiquitination. *Cell Biochem. Biophys.* 60:39-46. http://doi.org/10.1007/s12013-011-9181-9

Wu, Y.C., G.M. Stanfield, and H.R. Horvitz. 2000. NUC-1, a caenorhabditis elegans DNase II homolog, functions in an intermediate step of DNA degradation during apoptosis. *Genes Dev.* 14:536-548.

Xie, F., X. Zhou, H. Li, P. Su, S. Liu, R. Li, J. Zou, X. Wei, C. Pan, Z. Zhang, M. Zheng, Z. Liu, X. Meng, H. Ovaa, P. Ten Dijke, F. Zhou, and L. Zhang. 2022. USP8 promotes cancer progression and

extracellular vesicle-mediated CD8+ T cell exhaustion by deubiquitinating the TGF-beta receptor TbetaRII. *EMBO J.* 41:e108791. https://doi.org/10.15252/embj.2021108791

Xiong, W., X. Gao, T. Zhang, B. Jiang, M.M. Hu, X. Bu, Y. Gao, L.Z. Zhang, B.L. Xiao, C. He, Y. Sun, H. Li, J. Shi, X. Xiao, B. Xiang, C. Xie, G. Chen, H. Zhang, W. Wei, G.J. Freeman, H.B. Shu, H. Wang, and J. Zhang. 2022. USP8 inhibition reshapes an inflamed tumor microenvironment that potentiates the immunotherapy. *Nat. Commun.* 13:1700. http://doi.org/10.1038/s41467-022-29401-6

Yang, C., and X. Wang. 2021. Lysosome biogenesis: Regulation and functions. *J. Cell Biol.* 220:e202102001. http://doi.org/10.1083/jcb.202102001

Yong, X., G. Jia, Z. Liu, C. Zhou, J. Yi, Y. Tang, L. Chen, L. Chen, Y. Wang, Q. Sun, D.D. Billadeau, Z. Su, and D. Jia. 2023. Cryo-EM structure of the Mon1-Ccz1-RMC1 complex reveals molecular basis of metazoan RAB7A activation. *Proc. Natl. Acad. Sci. USA*. 120:e2301725120. https://doi.org/10.1073/pnas.2301725120

Zeigerer, A., J. Gilleron, R.L. Bogorad, G. Marsico, H. Nonaka, S. Seifert, H. Epstein-Barash, S. Kuchimanchi, C.G. Peng, V.M. Ruda, P. Del Conte-Zerial, J.G. Hengstler, Y. Kalaidzidis, V. Koteliansky, and M. Zerial. 2012. Rab5 is necessary for the biogenesis of the endolysosomal system in vivo. *Nature*. 485:465-470. https://doi.org/10.1038/nature11133

Zhang, J., J. Du, C. Lei, M. Liu, and A.J. Zhu. 2014a. Ubpy controls the stability of the ESCRT-0 subunit Hrs in development. *Development*. 141:1473-1479. https://doi.org/10.1242/dev.099564

Zhang, Z., T. Zhang, S. Wang, Z. Gong, C. Tang, J. Chen, and J. Ding. 2014b. Molecular mechanism for Rabex-5 GEF activation by Rabaptin-5. *Elife*. 3. 10.7554/eLife.02687

Zhu, H., G. Zhu, J. Liu, Z. Liang, X.C. Zhang, and G. Li. 2007. Rabaptin-5-independent membrane targeting and Rab5 activation by Rabex-5 in the cell. *Mol. Biol. Cell*. 18:4119-4128. https://doi.org/10.1091/mbc.e07-02-0100

Figure Legends

Figure 1. Abnormal lysosome morphology and enlarged MVB-like structures in *usp-50* mutants.

(A-C) Confocal fluorescence images of hypodermal cell 7 (hyp7) expressing the LAAT-1::GFP marker to highlight lysosome structures in L4 stage, young adult and 3-day-old adult animals. Scale bar, 5 μm. (D) Quantification of the individual volume and total volume of LAAT-1::GFP vesicles in hyp7 of 3-day-old adults. 19 animals for wild-type, 16 animals for *usp-50(xd413)* and 13 animals for *usp-50(gk632973)* were quantified. *P* value ****<0.0001. One-way ANOVA with Tukey's test. (E and F) The lysosomal membrane marker LAAT-1::GFP co-localizes with the lysosomal hydrolase NUC-1::mCherry in both wild-type (E) and *usp-50(xd413)* (F) animals. Scale bar represents 5 μm for (E-F) and 2 μm for enlarged inserts. (G) Confocal fluorescence images of hypodermis expressing HGRS-1::GFP in L4 stage worms. Compared to wild type, HGRS-1::GFP signal is reduced in *usp-50(gk632973)* and *usp-50(xd413)* animals. Scale bar: 5 μm. (H) Confocal fluorescence images of hypodermis expressing STAM-1::GFP in L4 stage worms. Compared to wild type, STAM-1::GFP signal is reduced in *usp-50(xd413)* animals. Scale bar: 5 μm. (I and I') High-pressure freezing EM reveals the MVB structure in wild-type animals. The yellow boxed area is enlarged in (I'). (J) Quantification of the vesicle size of MVB-like structures in wild-type and *usp-50(xd413)* animals. Data are presented as mean ±SEM. ***P<0.001. Unpaired Student's t-test was performed. (K-N) The enlarged abnormal vesicles in *usp-50(xd413)*, including vesicles containing abundant ILVs (58.7%) (K), vesicles filled with threadlike

membrane structures (26.8%) (L), vesicles loaded with electron-dense material (22.4%) (M), and vesicles containing various cellular organelles (4.9%) (N). Red dashed lines indicate hypodermal cells. Yellow arrows indicate representative vesicles. mito, mitochondrion. Scale bar: 0.5 μm for (I-N).

Figure 2. Enlarged EEs in *usp-50/usp8* mutant cells.

(A) Confocal fluorescence images of hypodermis expressing YFP::2xFYVE to detect EEs in L4 stage animals. Compared to wild-type, EEs are enlarged in *usp-50(gk632973)* and *usp-50(xd413)* mutants. Scale bar: 5 μm. (B) Quantification of the individual vesicle size, total volume, and number of YFP::2xFYVE-marked vesicles in hyp7 in L4 worms (10 animals for wild-type, 11 animals for *usp-50(gk632973)*, 13 animals for *usp-50(xd413)*). Data are presented as mean ± SEM. *P<0.05. **P<0.01. ***P<0.001. ****P<0.0001. ns, not significant; one-way ANOVA with Tukey's test. (C-D) The YFP::2xFYVE marker is not co-localized with LAAT-1::mCherry in wild-type (C) or *usp-50(xd413)* animals (D). Scale bar represents 5 μm for (C-D) and 2 μm for enlarged inserts. (E-J) The YFP::2xFYVE pattern in wild-type (E), *usp-50(xd413)* mutants (F), *usp-50(xd413)* with hypodermis-specific USP-50 expression (G), *usp-50(xd413)* with muscle-specific USP-50 expression (H), *usp-50(xd413)* with gut-specific USP-50 expression (I), and *usp-50(xd413)* with expression of human USP8 driven by the *usp-50* promoter (J). Scale bar: 5 μm. (K) Distribution of transiently expressed EGFP-2xFYVE in wild-type and USP8-KO SUM159 cells. Both wild-type and USP8-KO SUM159 cells were transiently transfected with EGFP-2xFYVE and then imaged by

spinning-disk confocal microscopy. The right panel shows quantification of the number of large endosomes marked by EGFP-2xFYVE from 38 cells for wild-type and 51 cells for USP8-KO (****P<0.0001 using an unpaired, two-sample Student's test). Scale bar: 10 μm.

Figure 3. USP8 is recruited to Rab5-positive vesicles.

(A-C) SUM159 cells genome-edited for USP8-mEGFP$^{+/+}$ were transiently transfected with the indicated mScarlet-I-tagged proteins and then imaged by spinning-disk confocal microscopy. The single-frame image in the figure shows the distribution of USP8 with EEA1, RAB7a, or Lamp1. USP8-mEGFP is co-localized with the early endosome marker mScarlet-EEA1 in genome-edited USP8-mEGFP$^{+/+}$ SUM159 cells (A). USP8-mEGFP is partly co-localized with the late endosome marker mScarlet-Rab7a (B) or the lysosome marker Lamp1-mScarlet-I (C). Scale bar represents 10 μm for (A-C) and 2 μm for enlarged inserts. (D) USP8-mEGFP localization on enlarged EEs in the genome-edited SUM159 cells. SUM159 cells genome-edited for USP8-mEGFP$^{+/+}$ were transiently transfected with mScarlet-I-EEA1 and Halo-Rab5c-Q80L, labeled with the JF_{646}-HaloTag ligand, and then imaged by spinning-disk confocal microscopy. Scale bar represents 10 μm for (D) and 2 μm for enlarged inserts. (E) SIM images showing the sub-organelle localization of USP8-mEGFP on EEs marked with mScarlet-EEA1. USP8-mEGFP$^{+/+}$ cells were transiently transfected with mScarlet-I-EEA1 and then imaged near the middle plane by SIM. Scale bar represents 2 μm for the left panels and 0.5 μm for the right enlarged panel. (F) SUM159 cells genome-edited

for USP8-mEGFP$^{+/+}$ were transiently transfected with mScarlet-I-Rab5c and then imaged at two planes (starting from the bottom plane, spaced by 0.5 μm) every 2 s (for 1 min) by spinning-disk confocal microscopy. Shown is the first frame of the maximum intensity projection of the two planes. The boxed region is enlarged and the images at the indicated times are shown on the right. Scale bar represents 10 μm for the left images and 2 μm for the right enlarged images. (G) Kymographs along the line (width 3 pixels) on the first merged image of the montage in (F) showing dynamic recruitment of USP8-mEGFP to the pre-existing mScarlet-Rab5-positive vesicles. (H) The time lapse images in (F) were analyzed by single-particle tracking. The trajectories (longer than 20 s, color-coded based on track lifetime) of Rab5c are plotted on the first frame of mScarlet-I-Rab5c. The boxed region is enlarged and shown on the right. The fluorescence intensity traces for mScarlet-I-Rab5c (red) and USP8-mEGFP (green) of the three tracked events are shown. Scale bar: 2 μm.

Figure 4. USP-50 interacts with RABX-5.

(A) The affinity-purified RABX-5::GFP from worm lysates is immuno-precipitated by USP-50::4xFLAG purified from KEK293T cells using anti-FLAG beads. Only the area of the blot containing the USP-50::4xFLAG band is displayed. (B) The affinity-purified USP-50::4xFLAG from KEK293T cells is immuno-precipitated by RABX-5::GFP purified from worm lysates using anti-GFP beads. N2 is wild-type. (C) Schematic drawing of RABX-5 showing the domains that interact with USP-50. (D) Immuno-precipitation tests between USP-50::MYC and FLAG-tagged truncated RABX-5. USP-

50::MYC and FLAG-tagged truncated RABX-5 were expressed via co-transfection into HEK293T cells, immunoprecipitated with FLAG beads and immunoblotted with antibodies against MYC and FLAG. (E) Schematic drawing of the RABX-5 protein structure. The molecular lesions of the null mutant is indicated. (F) Confocal fluorescence images of hyp7 expressing USP-50::GFP in wild-type L4 animals (*wt*), *rabx-5(null)* L4 mutants. Scale bar represents 5 μm. (G) Line scan analyses show the fluorescence intensity values along the red solid lines in (F).

Figure 5. USP-50 dissociates RABX-5 from endosomes

(A-D) The punctate distribution of RABX-5::GFP KI (knock-in) in wild type (A) and *usp-50(xd413)* (B). The increased RABX-5::GFP KI signal in *usp-50(xd413)* is rescued by expressing wild-type (C) but not C492A mutant *usp-50* (D). (E and F) The *usp-50(xd413)* mutation increases the GFP intensity of RABX-5(K88R)::GFP KI. (G and H) The *usp-50(xd413)* mutation does not alter the GFP intensity of RABX-5(K323R)::GFP KI. (I) Line scan analyses show the fluorescence intensity values along the red solid lines in (A-H). (J and K) Both the enlarged early endosome (YFP::2xFYVE) and the diminished late endosome (NUC-1::mCherry) phenotypes of *usp-50(xd413)* can be suppressed by *rabx-5(k323R)*. (L-M) Quantification of the volume of individual EEs (labeled by YFP::2xFYVE) and LEs (labeled by NUC-1::mCherry) in various genotypes. Data are presented as mean ± SEM. ****$P<0.0001$. ns, not significant; one-way ANOVA with Tukey's test. Scale bar represents 10 μm for (A-H), 5 μm for (J and K).

Figure 6. Loss of *usp-50/usp8* disrupts SAND-1/Mon1 localization

(A-C) The reduction of punctate GFP::SAND-1 signals in *rabx-5(null)* and *usp-50(xd413)* mutant animals. (D) Line scan analyses for (A-C). (E-G) The reduced lysosomes (labeled by LAAT-1::GFP) in *rabx-5(null)* and *usp-50(xd413)* mutant animals. (H-I) SUM159 cells genome-edited for mEGFP-Mon1a$^{+/+}$ (H) or mEGFP-Mon1b$^{+/+}$ (I) were treated with control siRNA or siRNA targeting USP8 and then imaged by spinning-disk confocal microscopy (starting from the bottom plane, spaced by 0.35 μm). The single frame image shows the distribution and area of Mon1a- or Mon1b-labeled endosomes near the middle plane. Quantification is shown on the right (Data are presented as mean ± SEM. ****P<0.0001; unpaired Student's t-test). Scale bar: 10 μm. (J-L) EEs (labeled by YFP::2xFYVE) are enlarged in *sand-1(or552)* mutants. (M-O) Late endosomes/lysosomes (labeled by LAAT-1::GFP) are smaller in *sand-1(or552)* mutants. (P) USP-50::MYC and SAND-1::4xFLAG were expressed in HEK293T cells via co-transfection, then immunoprecipitated with anti-FLAG beads and immunoblotted with antibodies against MYC and FLAG. (Q-S) The reduction of punctate GFP::RAB-7 signals in *sand-1(or522)* and *usp-50(xd413)* animals. (T) Line scan analyses for (Q-S). (U-W) Overexpressing *rab-7* suppresses the enlarged early endosome phenotype of *usp-50* mutants. EEs were detected with YFP::2xFYVE. (X) Quantification of the individual volume of YFP::2xFYVE vesicles in hypodermal cell 7 (hyp7) of L4 stage from 10 animals for wild-type, 13 animals for *usp-50(xd413)*, and 10 animals for the *rab-7*-expressing line (Data are presented as mean ± SEM.

****P<0.0001; one-way ANOVA with Tukey's test). (Y) Working models showing the role of USP-50 in endosome maturation. RABX-5-depdendent recruitment of USP-50 promotes the dissociation of RABX-5 from EEs and enhances the recruitment of SAND-1, thereby promoting the endosome maturation process. Scale bar represents 5 μm for (A-C, E-G, J-L, M-O, Q-S, U-W), 10 μm for (H and I).

Figure Legends for Supplementary Figures

Figure 1-figure supplement 1. ESCRT-0 components are stabilized by *usp-50*.

(A) Pearson's correlation coefficient for co-localization of the lysosome membrane protein LAAT-1 (LAAT-1::GFP) and the lysosomal nuclease NUC-1 (NUC-1::mCherry) in wild-type and *usp-50(xd413)* animals. ns, not significant. Unpaired Student's t-test was performed. (B) Quantification of the individual volume, total volume, and number of HGRS-1::GFP puncta in hypodermal cell 7 (hyp7) of L4 stage from 10 animals for wild-type, *usp-50(gk632973)* and *usp-50(xd413)* respectively. (Data are presented as mean ± SEM. ****P<0.0001; one-way ANOVA with Tukey's test).

Figure 2-figure supplement 1. *usp-50* functions cell-autonomously.

(A) Pearson's correlation coefficient for co-localization of EEs (labeled with YFP::2xFYVE) and lysosomes (labeled with LAAT-1:: mCherry) in wild-type and *usp-50(xd413)* animals. ns, not significant. Unpaired Student's t-test was performed. (B) Quantification of the volume of individual EEs in various genotypes. Data are presented as mean ± SEM. ****P<0.0001. ns, not significant; one-way ANOVA with Tukey's test. (C) The CRISPR/Cas9 genome-editing tool was used to knock out the expression of USP8 (USP8-KO) in SUM159 cells. Knockout of USP8 was confirmed by western blot analysis using antibodies against USP8 and GAPDH.

Figure 2-figure supplement 2. Mutation of *usp-50* does not affect other organelles.

(A-C) In *usp-50* mutant animals, no obvious alterations are detected in Golgi apparatus

(MANS::GFP) (A), recycling endosomes (GFP::RME-1) (B) or retromers (VPS-29::GFP) (C). Confocal fluorescence images of the hypodermis were captured at L4 stage. Scale bars represent 5 μm.

Figure 3-figure supplement 1. The EE localization of USP-50 and USP8.

(A) USP-50::GFP is co-localized with mCherry::RAB-5 in hypodermal cell 7 (hyp7) of wild-type animals at L4 stage. (B) USP-50::GFP is not co-localized with mCherry::RAB-7 in hypodermal cell 7 (hyp7) of wild-type animals at L4 stage. (C) USP-50::GFP(C492A) is co-localized with mCherry::RAB-5 in hypodermal cell 7 (hyp7) and causes enlarged EEs. Scale bar represents 5 μm for (A-C) and 10 μm for enlarged inserts.

Figure 3-figure supplement 2. The generation of endogenous tagged USP8.

(A) CRISPR/Cas9 genome-editing strategy used to incorporate mEGFP at the C-terminus of USP8 in SUM159 cells. The target sequence at the genomic *USP8* locus recognized by the single-guide RNA is highlighted by the blue nucleotides. The stop codon TAA (red) and the site of mEGFP incorporation upon homologous recombination are highlighted. (B) Genomic PCR analysis showing biallelic integration of mEGFP into the *USP8* genomic locus to generate the clonal gene-edited cell line USP8-mEGFP$^{+/+}$. (C) Western blot analysis of cell lysates probed with antibodies for USP8 and GAPDH. The endogenous and mEGFP-tagged USP8 are indicated by arrows.

Figure 5-figure supplement 1. USP8 inhibits the EE localization of Rabex5.

(A) USP8-KO leads to enlarged EEs and enhanced Rabex5 (Rabex5-mEGFP$^{+/+}$) and Rab5 (mScarlet-I-Rab5c) signals. Rabex5-mEGFP$^{+/+}$ SUM159 cells with or without USP8 expression were transiently transfected with mScarlet-I-Rab5c and then imaged by spinning-disk confocal microscopy. Images show the intracellular distribution of Rabex5-mEGFP and mScarlet-I-Rab5c. Scale bar: 10 μm. (B) Quantification of the number of Rabex5-mEGFP spots in Rabex5-mEGFP$^{+/+}$ cells. 32 wild-type and 32 USP8-KO cells were scored (*P<0.05 using an unpaired, two-sample Student's test). (C) Quantification of the number of large Rabex5-mEGFP spots (diameter > 0.5 μm) in Rabex5-mEGFP$^{+/+}$ cells. 30 wild-type and 29 USP8-KO cells were scored (****P<0.0001 using an unpaired, two-sample Student's test). (D) Enlarged EEs in USP8-KO SUM159 cells contain both Rabex5 (detected via knock-in of Rabex5-mEGFP) and EEA1 (detected by anti-EEA1). The wild-type and USP8-KO Rabex5-mEGFP$^{+/+}$ cells were transiently immuno-stained by anti-EEA1 antibody, and then imaged by spinning-disk confocal microscopy. Scale bar: 10 μm. Enlarged inserts: 2 μm. (E) The CRISPR/Cas9 genome-editing tool was used to knock out of USP8 expression (USP8-KO) in Rabex5-mEGFP$^{+/+}$ SUM159 cells. Knockout of USP8 was confirmed by western blot analysis using antibodies against USP8 and GAPDH.

Figure 5-figure supplement 2. Loss of *usp-50/USP8* leads to more activated RAB-5.

(A-B) The GFP::RAB-5 KI signal in wild type (A) and *usp-50(xd413)* (B). Scale bar:

5 μm. (C) Quantification of the volume of individual RAB-5::GFP KI vesicles in L4 animals (10 animals for wild-type and 11 animals for *usp-50(xd413)*). Data are presented as mean ± SEM. ****P<0.0001. unpaired Student's t-test. (D) Quantification of the relative GFP::RAB-5 KI signal on membrane vs. cytosol in hypodermal cell 7 (hyp7) of L4 animals. 10 animals for wild-type, 10 animals for *usp-50(xd413)*. ***P<0.001; unpaired Student's t-test. (E) Coomassie blue staining of purified GST-EEA1-NT protein. (F) More GFP::RAB-5 is pulled down by GST-EEA1-NT protein in *usp-50(xd413)* mutants. (G) The GFP::RAB-5 protein level is increased in *usp-50(xd413)* mutants. (H) Quantification of GFP::RAB-5 protein level in wild-type and *usp-50(xd413)* mutant animals from three independent experiments. ****P<0.0001; unpaired Student's t-test. (I) Knockdown of USP8 (USP8-KD) leads to enlarged EEs in genome-edited SUM159 cells expressing EGFP-Rab5c$^{+/+}$. EGFP-Rab5c$^{+/+}$ cells were treated with control siRNA (NC) or siRNA targeting USP8, and then imaged by spinning-disk confocal microscopy. Scale bar: 10 μm. Enlarged insertions: 2 μm. (J) The numbers of Rab5c-positive endosomes in (I) with diameters greater than 1.5 μm were quantified in 30 cells of each genotype. Data are presented as mean ± SEM. ****P<0.0001; unpaired Student's t-test.

Figure 5-figure supplement 3. The ubiquitin modification sites on RABX-5

(A) Peptide sequences identified from the ubiquitination proteomics analysis. (B) The ubiquitinated sites of RABX-5 detected by ubiquitination proteomics analysis.

Figure 6-figure supplement 1. The distribution of endogenous Mon1a and Mon1b proteins.

(A) Quantification of the individual volume of LAAT-1::GFP vesicles in hyp7 of 3-day-old adults. Data are presented as mean ± SEM. ****P<0.0001; one-way ANOVA with Tukey's test. (B) Western blotting analysis of SUM159 cells genome-edited to express mEGFP-Mon1a$^{+/+}$ using antibodies against GFP and GAPDH. (C and D) Genome-edited mEGFP-Mon1a$^{+/+}$ SUM159 cells were transiently transfected with mScarlet-I-Rab5c (C) and mScarlet-I-Rab7a (D), and then imaged by spinning-disk confocal microscopy. mEGFP-Mon1a localizes to both EEs (mScarlet-I-Rab5c) and late endosomes (mScarlet-I-Rab7a). (E) Western blotting analysis of genome-edited mEGFP-Mon1b$^{+/+}$ SUM159 cells using antibodies against GFP and GAPDH. (F and G) mEGFP-Mon1b is not localized on EEs (E) but is localized on late endosomes (G). Genome-edited mEGFP-Mon1b$^{+/+}$ SUM159 cells were transiently transfected with mScarlet-I-Rab5c (F) and mScarlet-I-Rab7a (G), and then imaged by spinning-disk confocal microscopy. Scale bar represents 10 μm. (H) Quantification of the individual volume of YFP::2xFYVE vesicles in hypodermal cell 7 (hyp7) of L4 worms. 10 animals for wild-type, 13 animals for *usp-50(xd413)*, and 18 animals for *sand-1(or552)*. Data are presented as mean ± SEM. ****P<0.0001; one-way ANOVA with Tukey's test. (I) Quantification of the individual volume of LAAT-1::GFP vesicles in hyp7 of 3-day-old adults (19 animals for wild-type, 16 animals for *usp-50(xd413)*, and 13 animals for *sand-1(or552)*). Data are presented as mean ± SEM. ****P<0.0001; one-way ANOVA with Tukey's test.

Figure 1

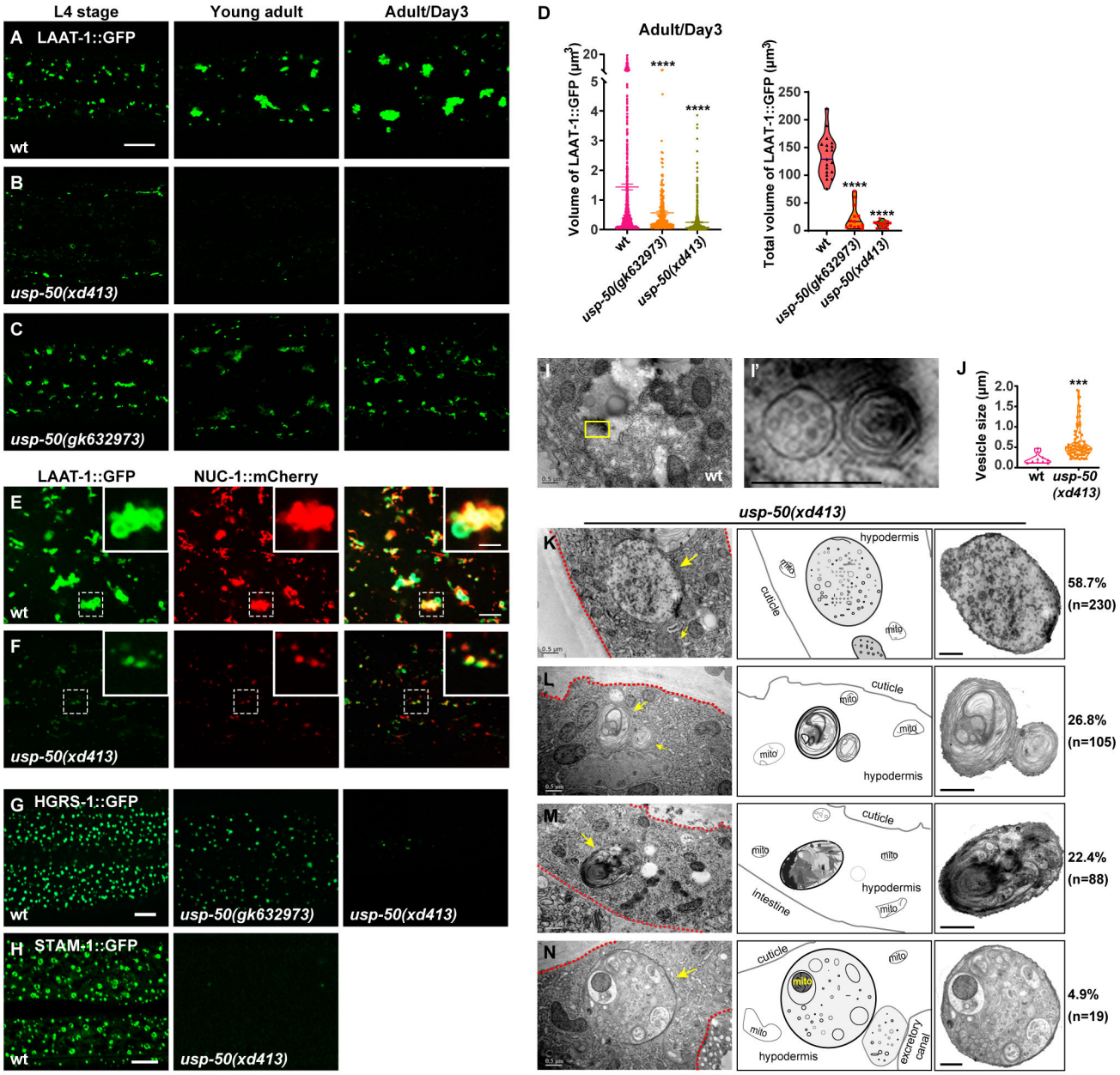
L4 stage
Young adult
Adult/Day3
A LAAT-1::GFP
wt
B
usp-50(xd413)
C
usp-50(gk632973)
LAAT-1::GFP
NUC-1::mCherry
E
wt
F
usp-50(xd413)
G HGRS-1::GFP
wt
usp-50(gk632973)
usp-50(xd413)
H STAM-1::GFP
wt
usp-50(xd413)
D
Adult/Day3
Volume of LAAT-1::GFP (μm³)
Total volume of LAAT-1::GFP (μm³)
****
wt
usp-50(gk632973)
usp-50(xd413)
I
I'
wt
J
Vesicle size (μm)
***
wt
usp-50 (xd413)
usp-50(xd413)
K
L
M
N
hypodermis
cuticle
mito
intestine
excretory canal
58.7%
(n=230)
26.8%
(n=105)
22.4%
(n=88)
4.9%
(n=19)

Figure 2

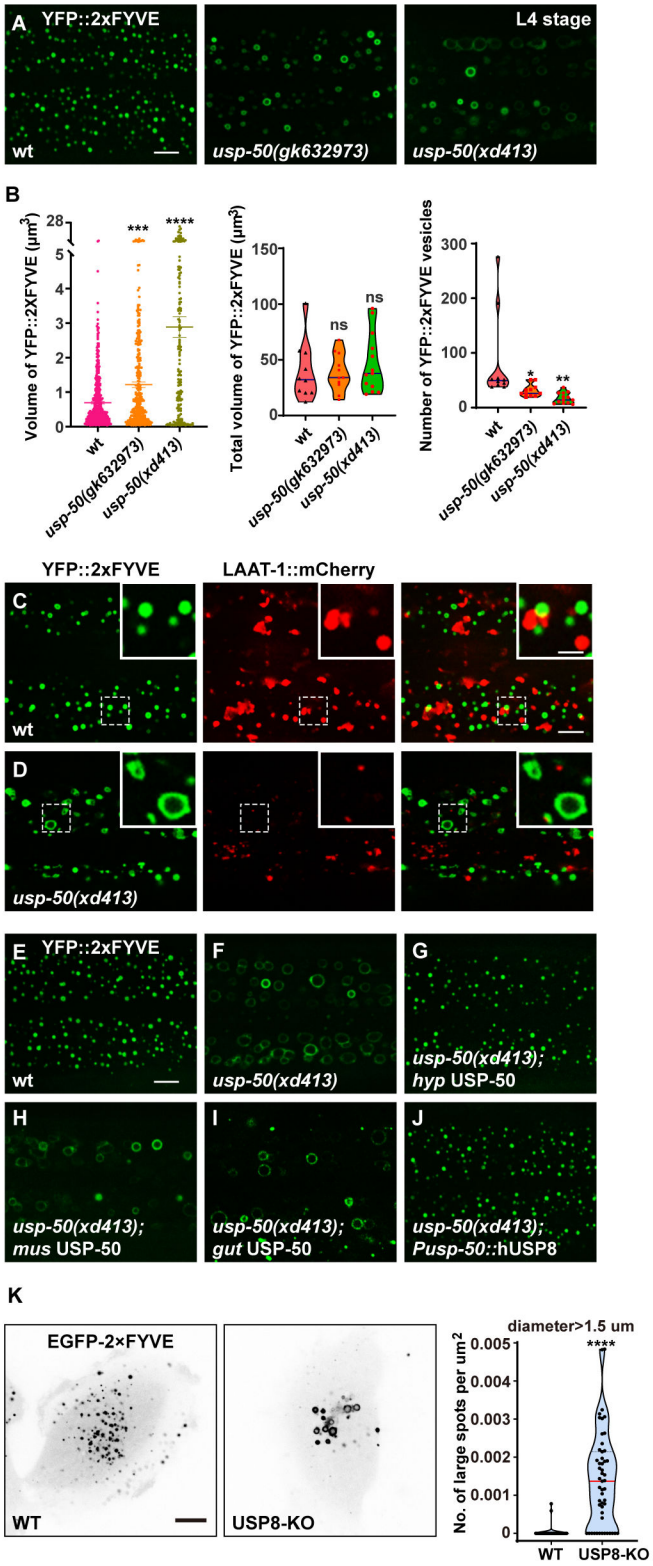
A
YFP::2xFYVE
L4 stage
wt
usp-50(gk632973)
usp-50(xd413)
B
Volume of YFP::2XFYVE (μm³)
Total volume of YFP::2xFYVE (μm³)
Number of YFP::2xFYVE vesicles
wt
usp-50(gk632973)
usp-50(xd413)
ns
YFP::2xFYVE
LAAT-1::mCherry
C
D
E
F
G
usp-50(xd413);
hyp USP-50
H
usp-50(xd413);
mus USP-50
I
usp-50(xd413);
gut USP-50
J
usp-50(xd413);
Pusp-50::hUSP8
K
EGFP-2×FYVE
WT
USP8-KO
diameter>1.5 um
No. of large spots per um²

Figure 3

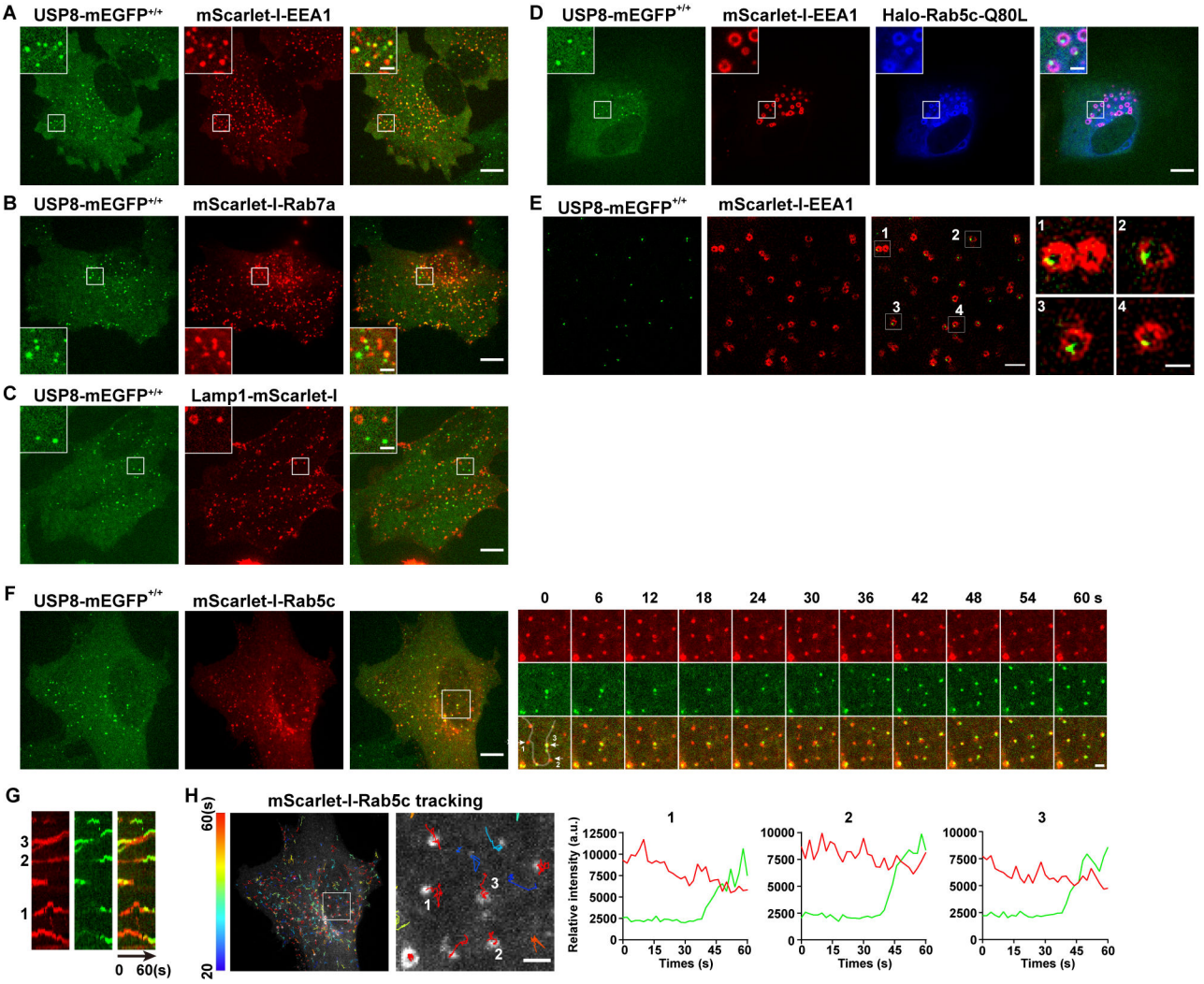
A
USP8-mEGFP+/+
mScarlet-I-EEA1
B
USP8-mEGFP+/+
mScarlet-I-Rab7a
C
USP8-mEGFP+/+
Lamp1-mScarlet-I
D
USP8-mEGFP+/+
mScarlet-I-EEA1
Halo-Rab5c-Q80L
E
USP8-mEGFP+/+
mScarlet-I-EEA1
F
USP8-mEGFP+/+
mScarlet-I-Rab5c
0 6 12 18 24 30 36 42 48 54 60 s
G
0 60(s)
H
mScarlet-I-Rab5c tracking
60(s)
20
Relative intensity (a.u.)
Times (s)

Figure 4

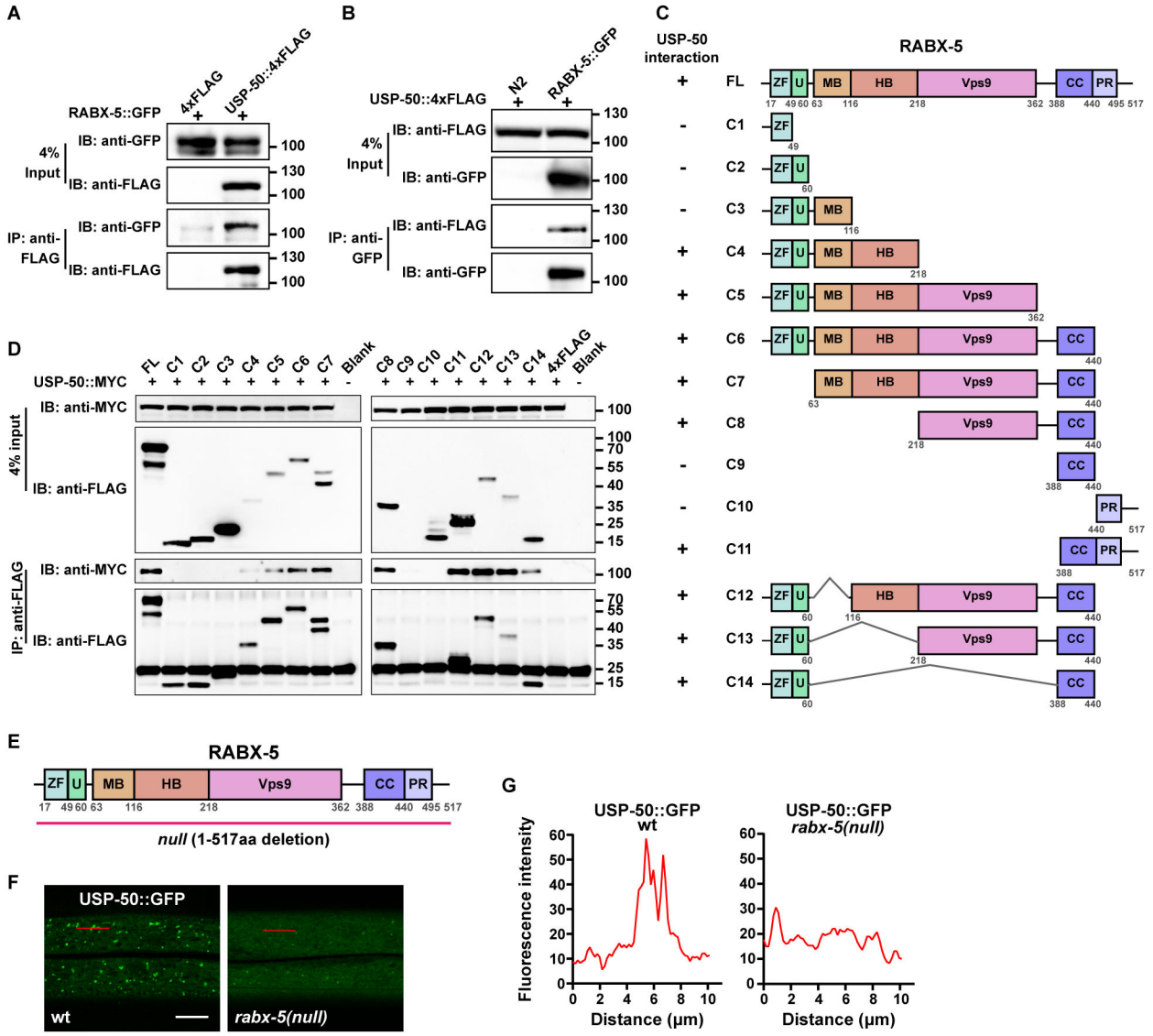
A
RABX-5::GFP
4xFLAG
USP-50::4xFLAG
4% Input
IB: anti-GFP
IB: anti-FLAG
IP: anti-FLAG
B
USP-50::4xFLAG
N2
RABX-5::GFP
IP: anti-GFP
C
USP-50 interaction
RABX-5
ZF
U
MB
HB
Vps9
CC
PR
D
USP-50::MYC
IB: anti-MYC
IB: anti-FLAG
IP: anti-FLAG
E
RABX-5
null (1-517aa deletion)
F
USP-50::GFP
wt
rabx-5(null)
G
USP-50::GFP wt
USP-50::GFP rabx-5(null)
Fluorescence intensity
Distance (μm)

Figure 5

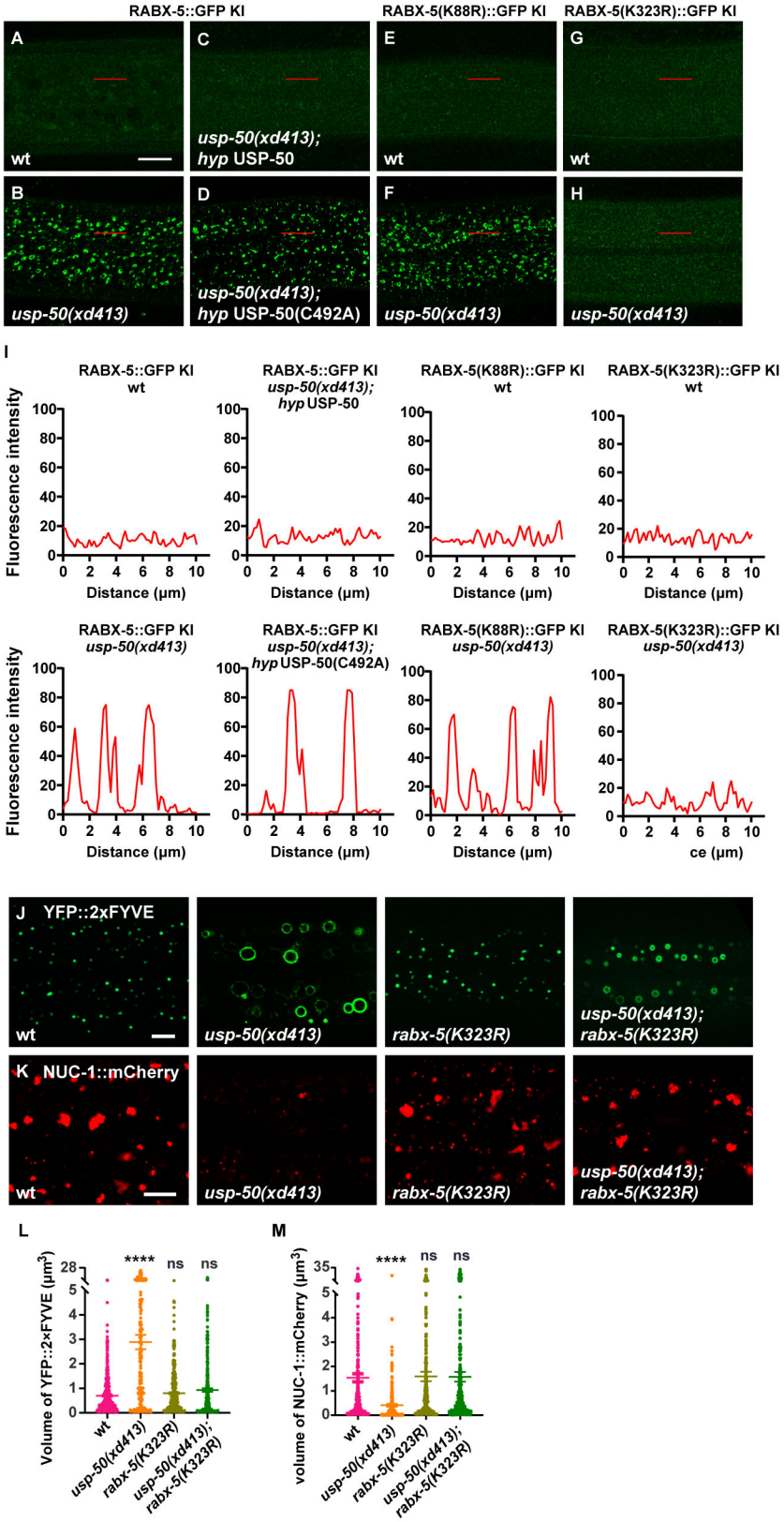
RABX-5::GFP KI
RABX-5(K88R)::GFP KI
RABX-5(K323R)::GFP KI
A
wt
C
usp-50(xd413);
hyp USP-50
E
wt
G
wt
B
usp-50(xd413)
D
usp-50(xd413);
hyp USP-50(C492A)
F
usp-50(xd413)
H
usp-50(xd413)
I
RABX-5::GFP KI
wt
RABX-5::GFP KI
usp-50(xd413);
hyp USP-50
RABX-5(K88R)::GFP KI
wt
RABX-5(K323R)::GFP KI
wt
Fluorescence intensity
Distance (μm)
RABX-5::GFP KI
usp-50(xd413)
RABX-5::GFP KI
usp-50(xd413);
hyp USP-50(C492A)
RABX-5(K88R)::GFP KI
usp-50(xd413)
RABX-5(K323R)::GFP KI
usp-50(xd413)
ce (μm)
J YFP::2xFYVE
wt
usp-50(xd413)
rabx-5(K323R)
usp-50(xd413);
rabx-5(K323R)
K NUC-1::mCherry
wt
usp-50(xd413)
rabx-5(K323R)
usp-50(xd413);
rabx-5(K323R)
L
Volume of YFP::2xFYVE (μm³)
****
ns
ns
wt
usp-50(xd413)
rabx-5(K323R)
usp-50(xd413);
rabx-5(K323R)
M
volume of NUC-1::mCherry (μm³)
****
ns
ns
wt
usp-50(xd413)
rabx-5(K323R)
usp-50(xd413);
rabx-5(K323R)

Figure 6

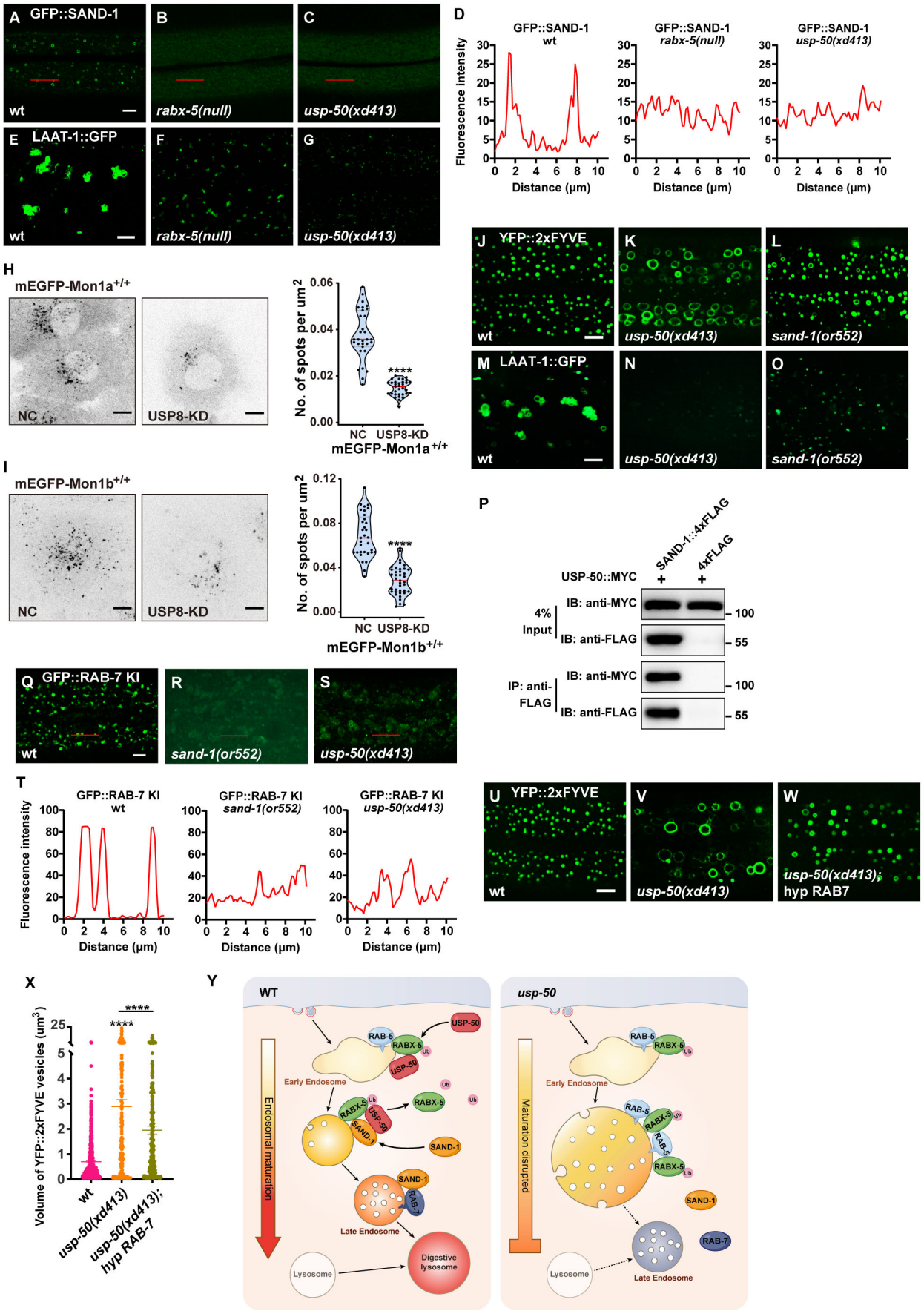
A GFP::SAND-1
wt
B
rabx-5(null)
C
usp-50(xd413)
E LAAT-1::GFP
wt
F
rabx-5(null)
G
usp-50(xd413)
D
GFP::SAND-1 wt
GFP::SAND-1 rabx-5(null)
GFP::SAND-1 usp-50(xd413)
Fluorescence intensity
Distance (μm)
H
mEGFP-Mon1a+/+
NC
USP8-KD
No. of spots per um2
****
NC USP8-KD
mEGFP-Mon1a+/+
I
mEGFP-Mon1b+/+
NC
USP8-KD
No. of spots per um2
****
NC USP8-KD
mEGFP-Mon1b+/+
J YFP::2xFYVE
wt
K
usp-50(xd413)
L
sand-1(or552)
M LAAT-1::GFP
wt
N
usp-50(xd413)
O
sand-1(or552)
P
SAND-1::4xFLAG
4xFLAG
USP-50::MYC
+
+
4% Input
IB: anti-MYC
IB: anti-FLAG
IP: anti-FLAG
IB: anti-MYC
IB: anti-FLAG
100
55
100
55
Q GFP::RAB-7 KI
wt
R
sand-1(or552)
S
usp-50(xd413)
T
GFP::RAB-7 KI wt
GFP::RAB-7 KI sand-1(or552)
GFP::RAB-7 KI usp-50(xd413)
Fluorescence intensity
Distance (μm)
U YFP::2xFYVE
wt
V
usp-50(xd413)
W
usp-50(xd413); hyp RAB7
X
Volume of YFP::2xFYVE vesicles (um3)
****
****
wt
usp-50(xd413)
usp-50(xd413); hyp RAB-7
Y
WT
usp-50
Endosomal maturation
Maturation disrupted
Early Endosome
Late Endosome
Lysosome
Digestive lysosome
RAB-5
RABX-5
USP-50
SAND-1
RAB-7
Ub

Figure 1-figure supplement 1

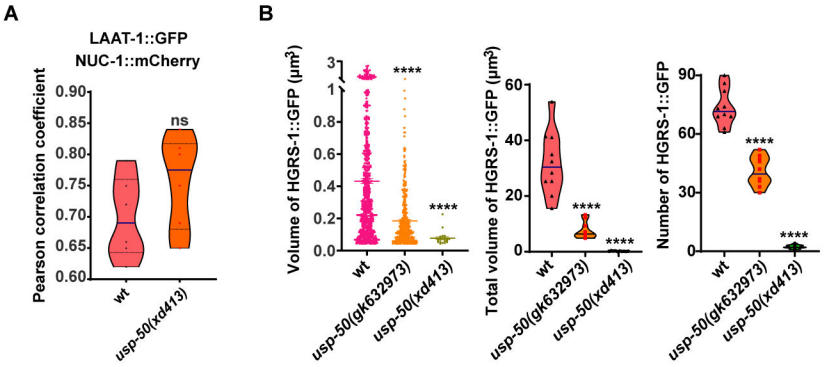

Figure 2-figure supplement 1

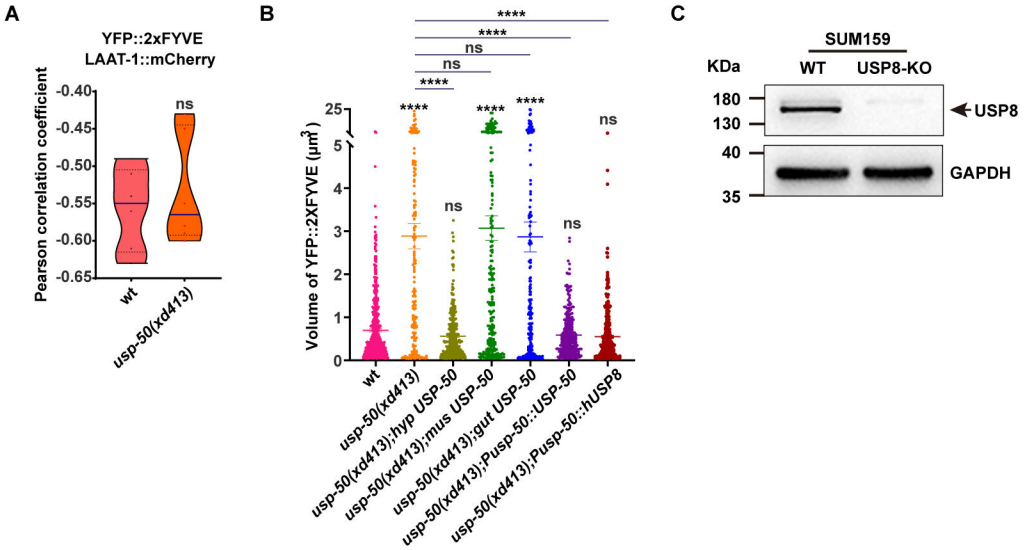

Figure 2-figure supplement 2

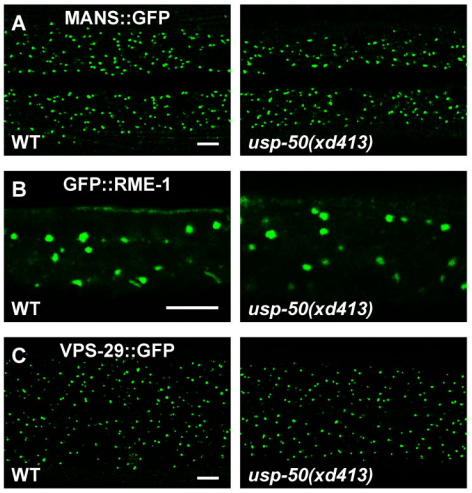

Figure 3-figure supplement 1

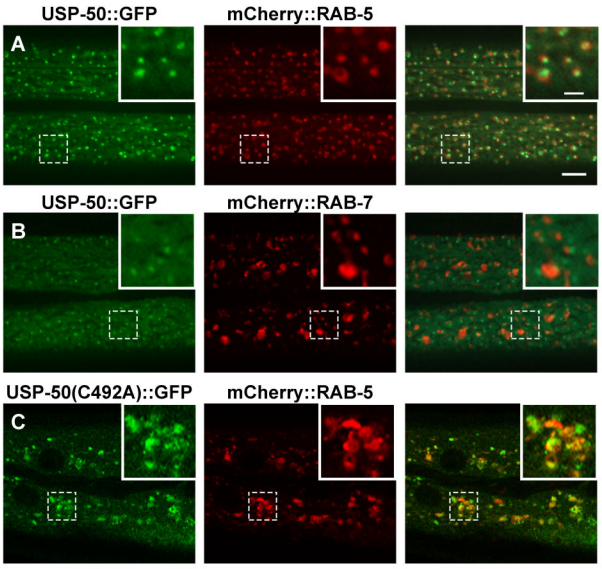

Figure 3-figure supplement 2

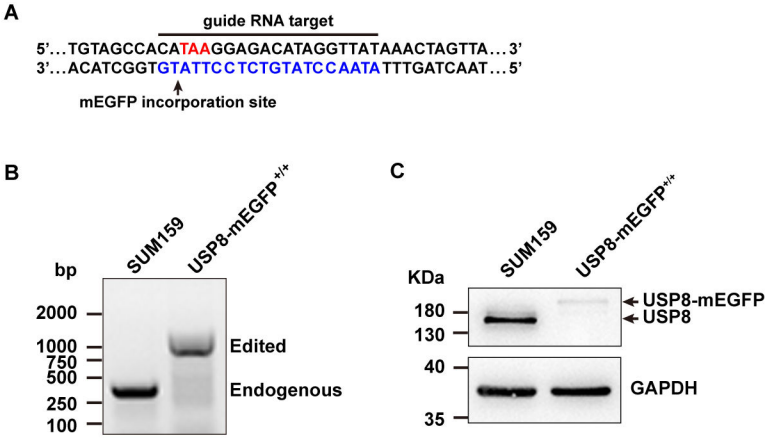

Figure 5-figure supplement 1

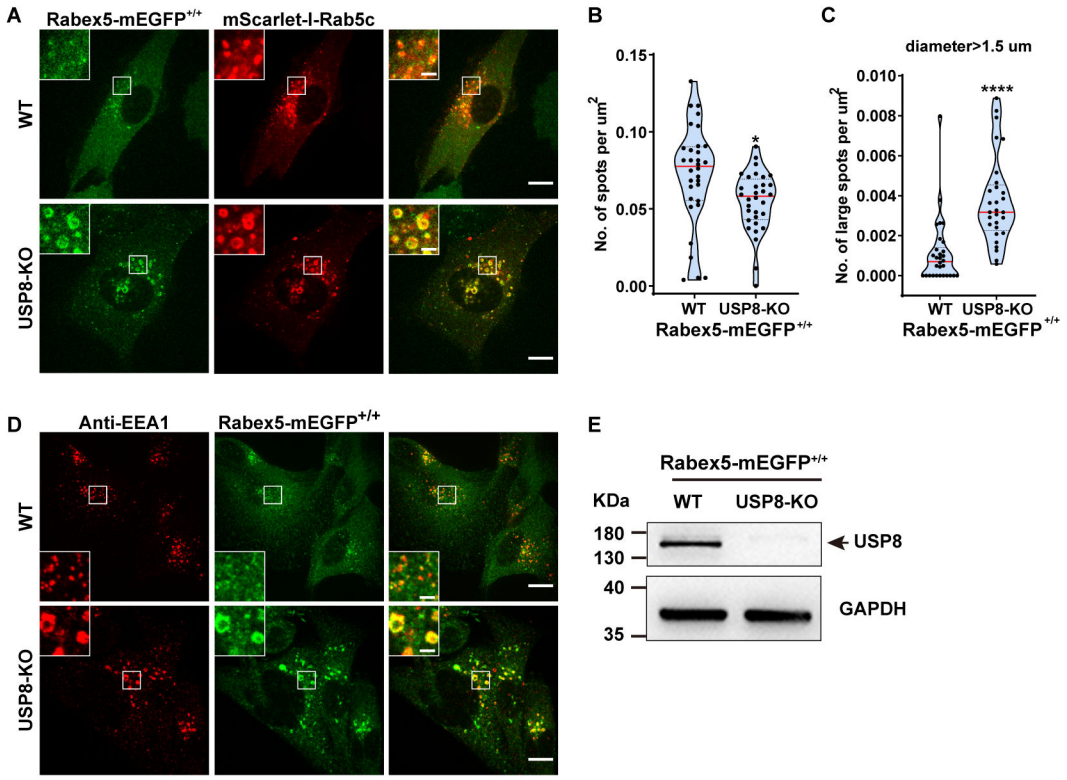

Figure 5-figure supplement 2

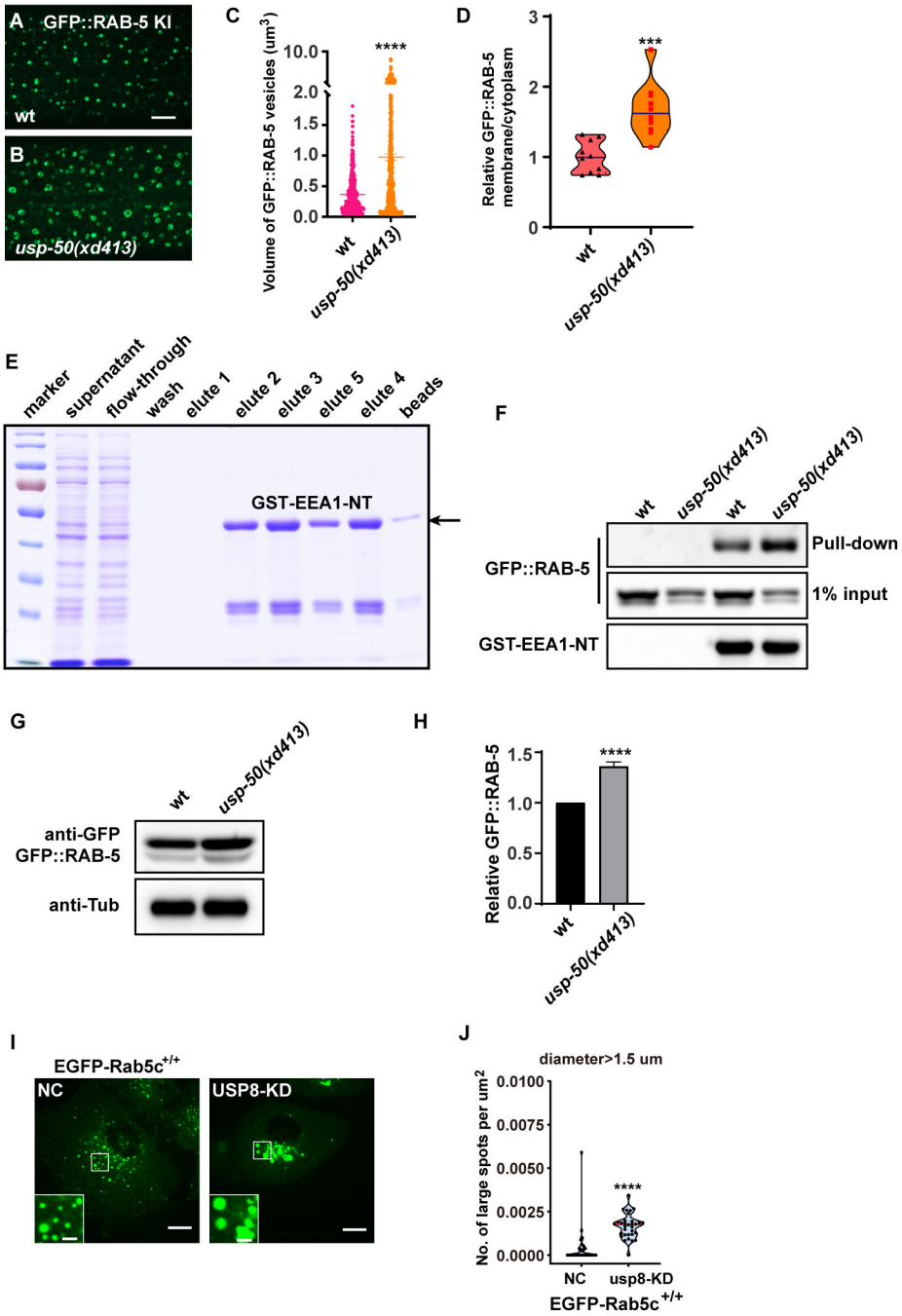

Figure 5-figure supplement 3

A

	Ubiquitinated site	Peptide sequence	Spectral hits
RABX-5::4×FLAG	K88	GIKNLFK^{GG}TSPIPEGGTSSPTSTSPAS	1
	K88	NLFK^{GG}TSPIPEGGTSSPTSTSPASTPT	1
	K323	GNPPLIQSNVK^{GG}FISR	2

B
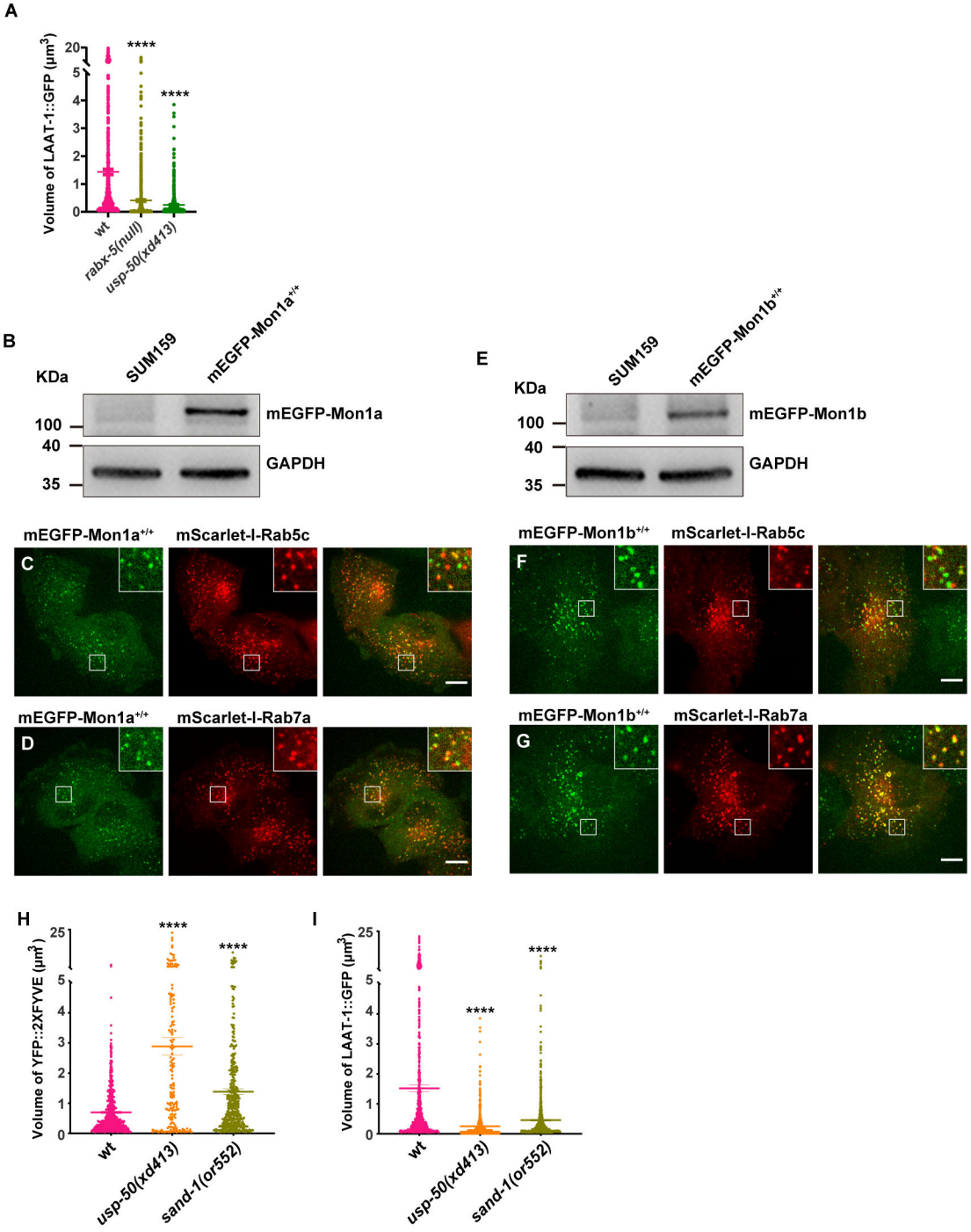
Figure 6-figure supplement 1